

Uplift Resistance of Anchor Plate Using Extended Mohr-Coulomb Model



Kyeong Sun Kim

Civil and Environmental Engineering

Seoul National University

November, 2021

Contents

1 Constitutive Model	2
1.1 Strain—Softening Stiffness—Hardening Model	3
1.1.1 Yield function	3
1.1.2 Plastic potential function	3
1.1.3 Hardening function	4
1.2 Nonassociated Flow Rule (NA)	5
1.3 Extended Mohr—Coulomb Model (EMC)	7
1.3.1 Comparison between associated and non-associated flow rule in plastic model	8
1.3.2 Yield function	9
1.3.3 Plastic potential function	9
1.3.4 Flow rule	10
1.3.5 Hardening	10
1.3.6 Soil Parameters	10
2 Calibration and Validation	12
2.1 Drained Triaxial Test	13
2.2 Soil Parameters	16
2.2.1 Strain—Softening Stiffness—Hardening Model	16
2.2.2 Nonassociated Flow Rule (NA)	16
2.2.3 Extended Mohr—Coulomb Model (EMC)	17
2.3 Convergence Criteria	18
2.3.1 Mesh Convergence	18
2.3.2 Boundary Convergence	25
3 Results	28
3.1 Parametric Study	28
3.1.1 Effect of Embedment Depth Ratio $\frac{D}{B}$	31

Contents

3.1.2	Effect of Width B	32
3.1.3	Shear Dissipation	32
3.2	Comparison with Previous Researchers	39
4	Comparison with Centrifuge Experiment	41
4.1	Comparison of the centrifuge test results with the chosen model . .	53
4.2	Difference with the anchor theory	56
Appendices		
A	List of Load—Displacement Curves	60
B	REFERENCES	67

Contents

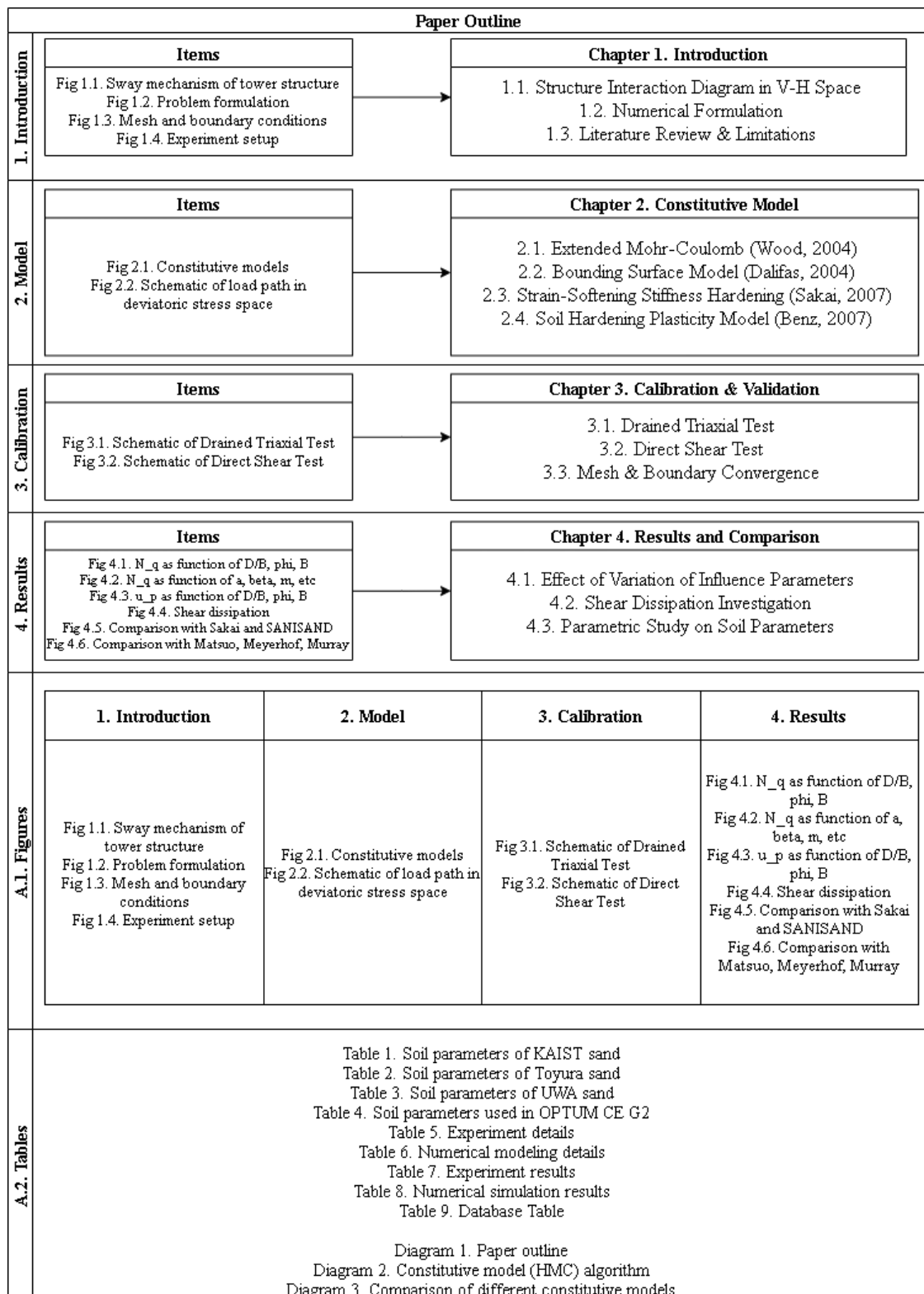


Figure 1: Paper Outline

1

Constitutive Model

Contents

1.1	Strain—Softening Stiffness—Hardening Model	3
1.1.1	Yield function	3
1.1.2	Plastic potential function	3
1.1.3	Hardening function	4
1.2	Nonassociated Flow Rule (NA)	5
1.3	Extended Mohr—Coulomb Model (EMC)	7
1.3.1	Comparison between associated and non-associated flow rule in plastic model	8
1.3.2	Yield function	9
1.3.3	Plastic potential function	9
1.3.4	Flow rule	10
1.3.5	Hardening	10
1.3.6	Soil Parameters	10

1. Constitutive models

Here is a brief description of the constitutive models:

1. Strain—Softening Stiffness—Hardening Model by Sakai and Tanaka, 1993
2. Typical Mohr-Coulomb with Non-associated Flow
3. Extended Mohr-Coulomb Model by David Muir Wood, 2004

1.1 Strain—Softening Stiffness—Hardening Model

It is assumed that the yield function F is defined by the stress $\vec{\sigma}$ and the soil parameter χ (Tanaka and Sakai, 1993):

$$F(\vec{\sigma}, \alpha(\chi)) = 0$$

In order to avoid numerical instability due to singularity of the non-associated Mohr-Coulomb model, a constitutive model based on the yield function of M-C type and the plastic potential function of Draker-Prager type is employed.

For predicting deformations in a post-peak regime, the elastic- strain-softening plastic model is developed. The yield function is given by the following expression.

1.1.1 Yield function

$$F(\vec{\sigma}, \alpha(\chi)) = 3\alpha(\chi)p' + \frac{\sqrt{J_2}}{g(\theta)} - c(\chi) = 0$$

1.1.2 Plastic potential function

$$G(\vec{\sigma}, \alpha'(\chi)) = 3\alpha'(\chi)p' + \sqrt{J_2} - c(\chi) = 0$$

$$\chi = \int \delta \varepsilon^p$$

$$(\delta \varepsilon^p)^2 = 2[(\delta \epsilon_x^p)^2 + (\delta \epsilon_y^p)^2 + (\delta \epsilon_z^p)^2] + (\delta \gamma^p)^2$$

, where

p' is mean stress,

J_2 is second invariant of deviatoric stress,

1. Constitutive models

χ is soil hardening parameter,

$c(\chi)$ is apparent cohesion function,

$\delta\varepsilon_{x,y,z}^p, \delta\gamma^p$ is incremental deviatoric plastic strains.

In case of the Mohr-Coulomb model, $g(\theta)$ is given by:

$$g(\theta) = \frac{3 - \sin\phi}{2\sqrt{3}\cos\theta - 2\sin\theta\sin\phi}$$

, where

θ is Lode angle; if triaxial compression, $= -30^\circ$

ϕ is mobilized internal friction angle.

1.1.3 Hardening function

The simple strain-softening functions are specified and expressed as a function of material constants. (Tanaka and Sakai, 1993)

$$\alpha(\chi) = \left(\frac{2\sqrt{a\chi}}{\chi + a} \right)^m \alpha_p \text{(hardening regime; } \chi \leq a)$$

$$\alpha(\chi) = \alpha_r + (\alpha_p - \alpha_r) \exp\left\{-\left(\frac{\chi - a}{b}\right)\right\} \text{(softening regime; } \chi > a)$$

, where

a, b, m are soil parameters.

Similar expressions are used by de Borst (1986).

$$\alpha_p = \frac{2\sin\phi_p}{\sqrt{3}(3 - \sin\phi_p)}$$

$$\alpha_r = \frac{2\sin\phi_r}{\sqrt{3}(3 - \sin\phi_r)}$$

, where

$\phi_{p,r}$ are peak and residual friction angle, respectively.

1. Constitutive models

1.2 Nonassociated Flow Rule (NA)

Since there may be a range of possible solutions, each associated with a different pattern of localization and all of which are entirely valid, it can be expected that any numerical solution will be very sensitive to both physical imperfections as well as round-off errors and the exact sequence in which the procedures defining the solution scheme are carried out. In the end, the result is a load-displacement response that tends to be rather oscillatory.

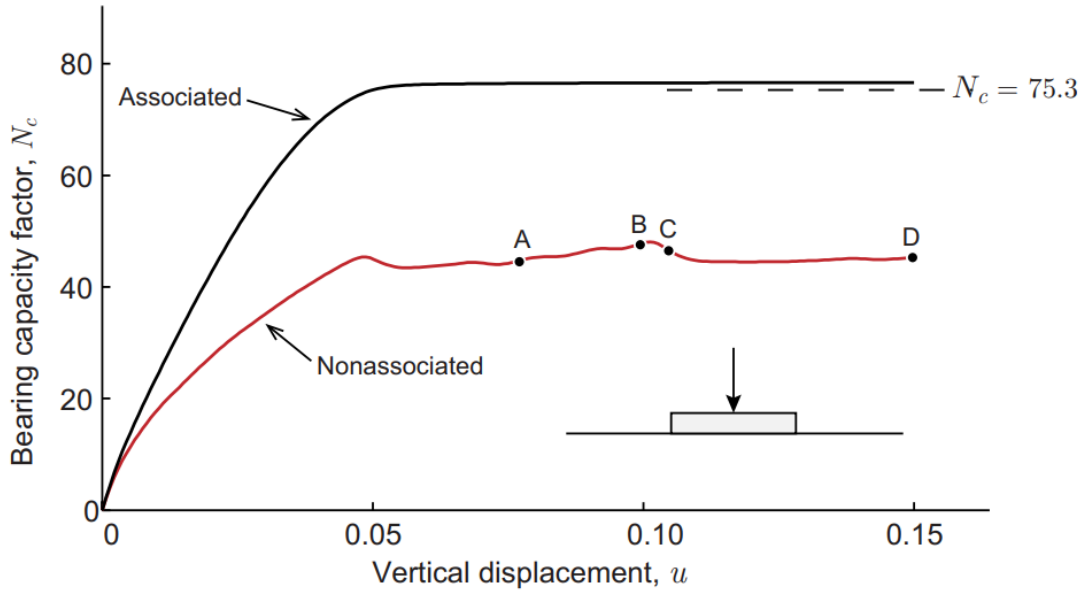


Figure 1.1: Load-displacement response for strip footing on a weightless soil (After Krabbenhoft et al., 2012)

The basic idea behind the formulation derives from the structure of the internal dissipation associated with constitutive models. Let us assume a yield function of the type:

$$F = Mp + q - c$$

, where

p and q are mean and deviatoric stress, M is a friction coefficient, and c is cohesion.

1. Constitutive models

The plastic potential function is given by:

$$G = Np + q$$

, where $N \leq M$ is a dilation coefficient.

In $p - q$ triaxial space, the plastic strain rates are given by:

$$\delta\varepsilon_v^p = \delta\lambda \frac{\partial G}{\partial p} = \delta\lambda N \delta\varepsilon_s^p = \delta\lambda \frac{\partial G}{\partial p} = \delta\lambda$$

, where δ denotes time increment, ε_v^p and ε_s^p are volumetric and deviatoric plastic strains conjugate to p and q , respectively.

The dissipation D is given by:

$$\begin{aligned} D &= p\varepsilon_v^p + q\varepsilon_s^p \\ &= (Nq + q)\delta\lambda \\ &= [c - (M - N)p]\delta\lambda \\ &= [c - (M - N)p]\varepsilon_s^p \end{aligned}$$

The above-mentioned parameters are all related with the confining pressure, which can be easily illustrated with the figure below:

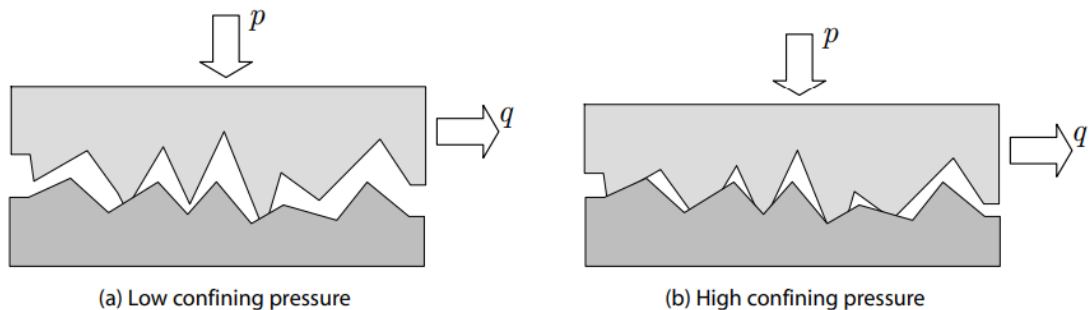


Figure 1.2: Microscopic origins of friction as plastic shearing of asperities. A higher confining pressure implies a higher degree of interlocking of the asperities and thereby a higher apparent shear strength (After Krabbenhoft et al., 2012)

1. Constitutive models

1.3 Extended Mohr—Coulomb Model (EMC)

The elastic-perfectly plastic Mohr-Coulomb model is widely used for geotechnical analysis. It provides very crude match to actual shearing behavior of soils. A natural extension is to create a hardening version of the M-C model in which the size of the yield surface varies in some nonlinear way with the development of plastic strain. In the model to be described as hardening will be linked only with distortional strain. It is useful for modelling sands , where it is rearrangement of the rather particles that dominates the response and irrecoverable volumetric changes are essentially linked by this rearrangement of particles (Wood, 2004).

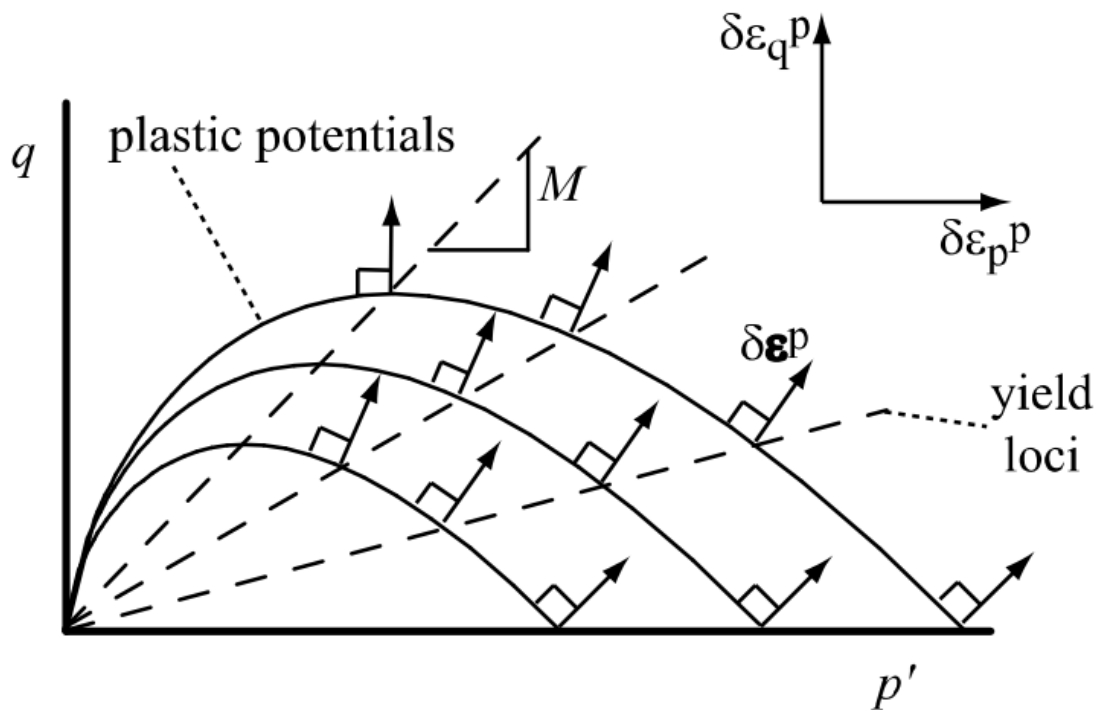


Figure 1.3: Plastic potential curves (solid lines) and yield loci (dashed lines) in elastic-hardening plastic Mohr-Coulomb model

Following Taylor's (1948) proposal of a link between dilatancy and mobilized friction in a shear box test, stress—dilatancy equation expressed in terms of total strain increments is obtained.

1. Constitutive models

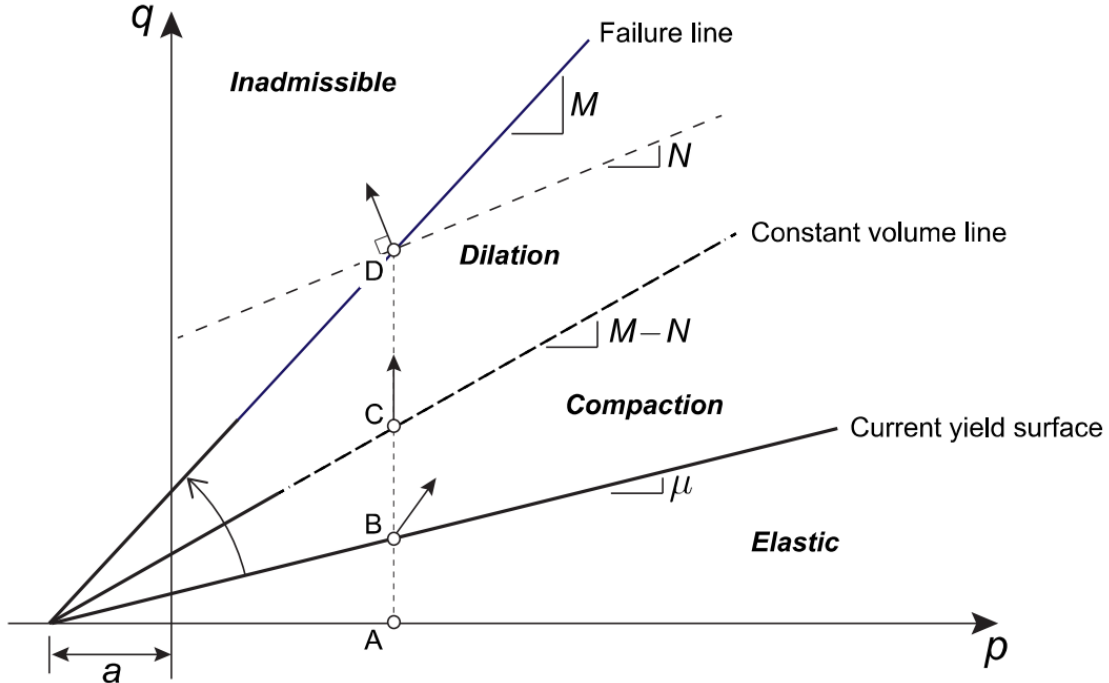


Figure 1.4: Hardening, compaction and dilation in the HMC model

1.3.1 Comparison between associated and non-associated flow rule in plastic model

In the elastic-perfectly-plastic Mohr-Coulomb model, it is commonly assumed that the plastic potential takes the same form as the yield surface, but with the slope defined by a dilation angle ψ rather than a friction angle. If this assumption is adopted, then the direction of the plastic strain increment $\delta\varepsilon^p$ would be normal to a set of parallel lines by the dilation angle. If normality rule were assumed, radical difference between the slope of yield criterion line and the plastic potential contour is observed (J.P. Doherty and D. Muir Wood, 2013).

1. Constitutive models

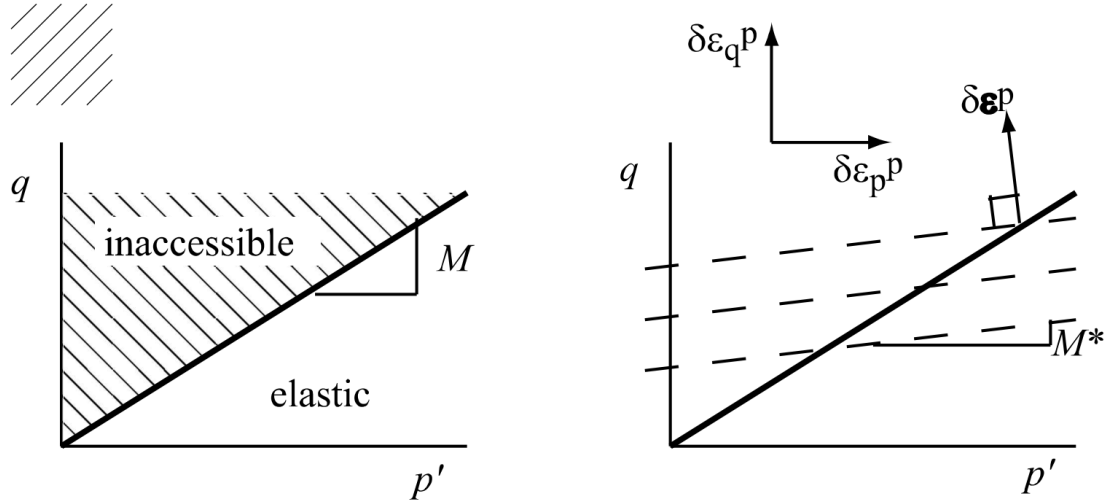


Figure 1.5: Elastic-perfectly plastic Mohr-Coulomb model (a) yield and failure locus, (b) plastic potentials

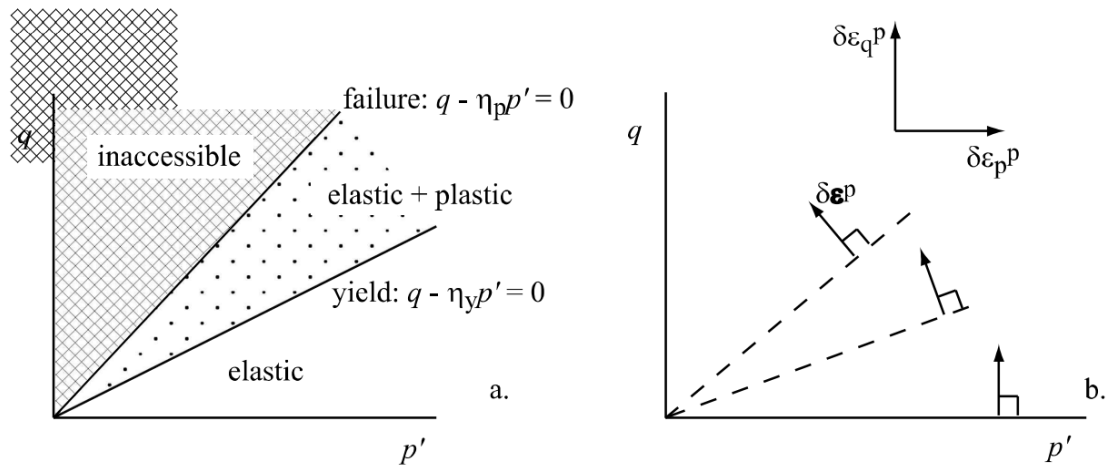


Figure 1.6: Elastic-hardening plastic Mohr-Coulomb model (a) yield locus and failure locus separating elastic plastic and inaccessible regions of stress plane (b) normality applied at the plastic region

1.3.2 Yield function

$$F(\vec{\sigma}, \chi) = F(p', q, \chi) = q - \eta_y p' = 0$$

1.3.3 Plastic potential function

$$G(\vec{\sigma}) = q - (M - M')p' \ln\left(\frac{p'_x}{p'}\right) = 0$$

1. Constitutive models

, where $\eta_{y,p}$ is stress ratio at yield and peak, respectively,

p'_r is chosen s.t. plastic potential gradient passes through current stress, i.e.,

$$p'_r = p' \exp\left\{\frac{\eta_y}{M-M'}\right\}$$

M is material parameter at perfect plasticity when hardening terminates.

$$M = \frac{6\sin\phi}{3-\sin\phi}$$

M' is dilation at constant volume line:

$$M' = \frac{6\sin\psi}{3-\sin\psi}$$

$$M' = M - k\psi = M - k(v - \Gamma + \lambda \ln p')$$

k is soil constant linking state variable and strength.

Critical State description is as follows:

$$M' = M - k[(v_0 - \Gamma + \lambda \ln p'_0 + (\lambda \ln \frac{p'}{p'_0} - v_0 \varepsilon_p^e) - v_0 \varepsilon_p^p)].$$

1.3.4 Flow rule

$$\frac{\delta \varepsilon_p^p}{\delta \varepsilon_q^p} = M - M' - \eta_y$$

1.3.5 Hardening

$$\delta \eta_y = \frac{1 - \frac{\eta_y}{M}}{\beta} \delta \varepsilon_q^p$$

, where

β is a model parameter scaling plastic strain,

$$\beta = \frac{3}{2} p' \frac{9-M}{9-(M-M')M \ln 2 - 3M'} \frac{1-E_{50}/E_{ur}}{E_{50}} \text{ for Taylor's } \sigma - \psi \text{ relation.}$$

The incremental of the stress ratio is defined as:

$$\delta \eta_y = \frac{3 \sin \delta \phi}{\sqrt{3} \cos \theta + \sin \theta \sin \delta \phi}$$

1.3.6 Soil Parameters

Elastic Moduli

The elastic moduli are estimated from the modified equation proposed by Hardin and Black (1968) in the case of sand:

1. Constitutive models

$$G = G_0 \frac{(2.17 - e)^2}{1 + e} \sqrt{p'} K = \frac{1 + \nu}{3(1 - 2\nu)} G$$

, where

ν is Poisson's ratio,

e is void ratio,

G_0 is initial shear modulus.

Peak friction angle

The peak friction angle of ϕ_p is estimated from the empirical relations proposed by Bolton (1987):

$$I_r = D_r [5 - \ln(\frac{p'}{150})] - 1, \quad (p' \geq 150 kN/m^2) \\ I_r = 5D_r - 1, \quad (p' < 150 kN/m^2) \\ \phi_p = 3I_r + \phi_r$$

Dilatancy angle

The dilatancy angle of ψ is estimated from modified Rowe's stress-dilatancy relationship:

$$\sin\psi = \frac{\sin\phi - \sin\phi'_r}{1 - \sin\phi \sin\phi'_r} \phi'_r = \phi_r [1 - \beta \exp\{-(\frac{\chi}{\epsilon_d})^2\}]$$

, where

β and ϵ_d are stress—dilatancy material parameters.

E_{50} is a secant modulus defined as:

$$E_{50} = \frac{\frac{1}{2}q_u}{\epsilon_{a,50}}$$

E_{ur} is unloading/reloading stiffness.

2

Calibration and Validation

Contents

2.1	Drained Triaxial Test	13
2.2	Soil Parameters	16
2.2.1	Strain—Softening Stiffness—Hardening Model	16
2.2.2	Nonassociated Flow Rule (NA)	16
2.2.3	Extended Mohr—Coulomb Model (EMC)	17
2.3	Convergence Criteria	18
2.3.1	Mesh Convergence	18
2.3.2	Boundary Convergence	25

For the validity of the finite element tests performed, the triaxial elemental test is simulated with the box of union length. The set up is as follows:

2. Calibration

2.1 Drained Triaxial Test

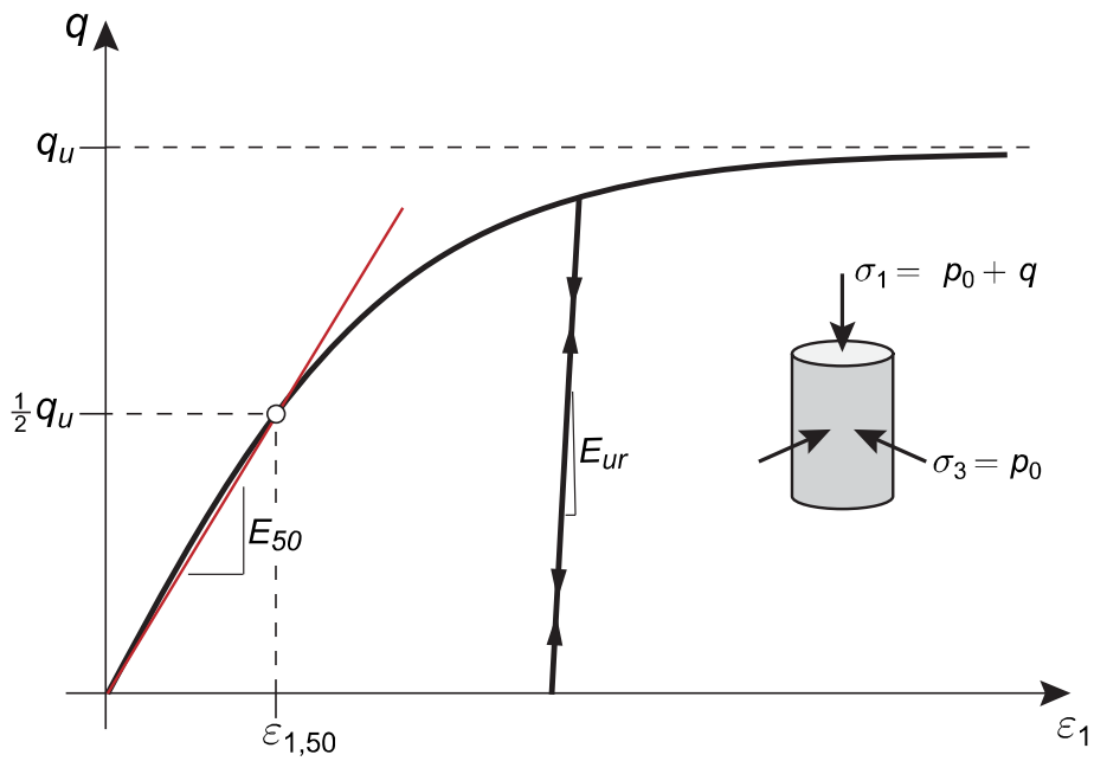


Figure 2.1: Typical triaxial test (After Krabbenhoft, 2013)

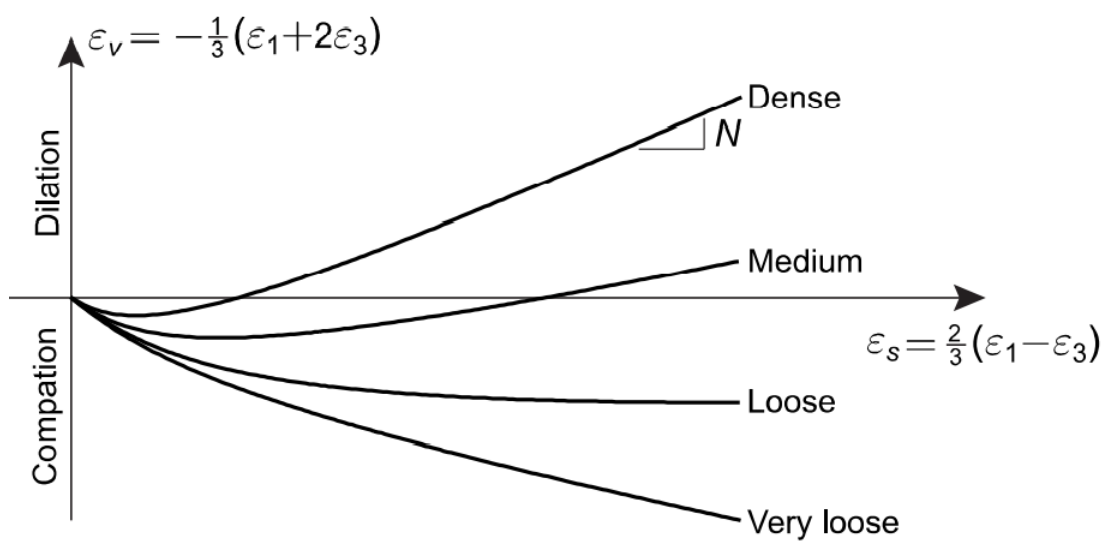


Figure 2.2: Typical shear-volumetric strain behavior in triaxial compression (After Krabbenhoft, 2013)

2. Calibration

Two tests — Triaxial compression and extension (TC/TE) — are simulated using Multiplier Elasto—plastic analysis under axisymmetric conditions as indicated in the Figure below. The fixed loads here represent the initial axial and radial stresses while the axial Multiplier load is increased in the course of the analysis to reach the ultimate limit state.

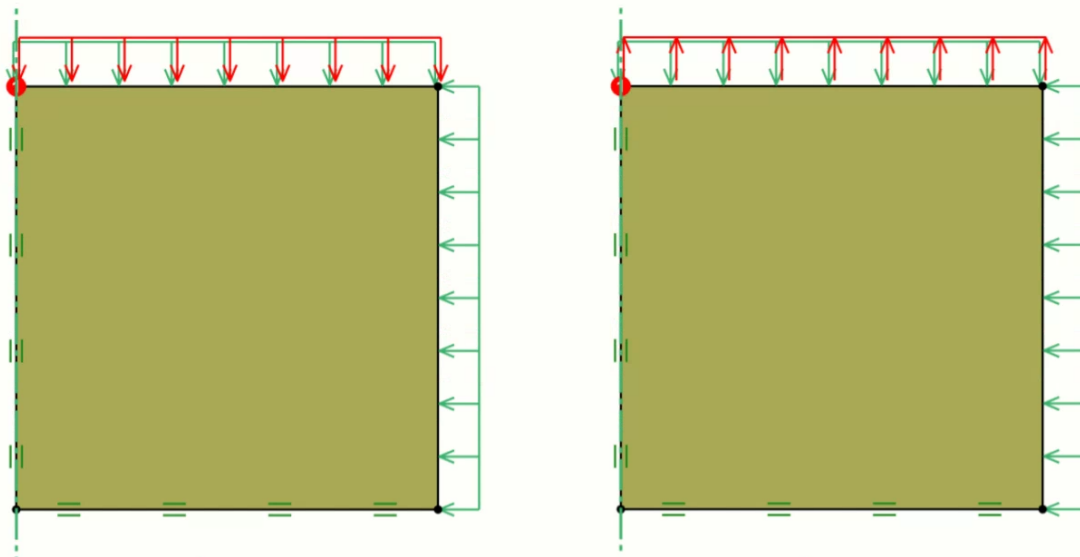


Figure 2.3: Setup for elemental triaxial compression and extension

By a process of trial and error, the fits shown in Figure are obtained. For this data set , where no information about the behavior in simple shear is available the value is well within range that can be accommodated by the isotropic strength option, there is little reason to assume any anisotropy. We note that the compression secant modulus in compression is only half of the extension secant modulus. This is somewhat unusual, but in this case nevertheless what fits the data best.

Result of Elemental Triaxial Test at 100 kPa

Triaxial test at radial stress of 100 kPa is simulated using one by one block of the finite element formulation with the EMC model.

2. Calibration

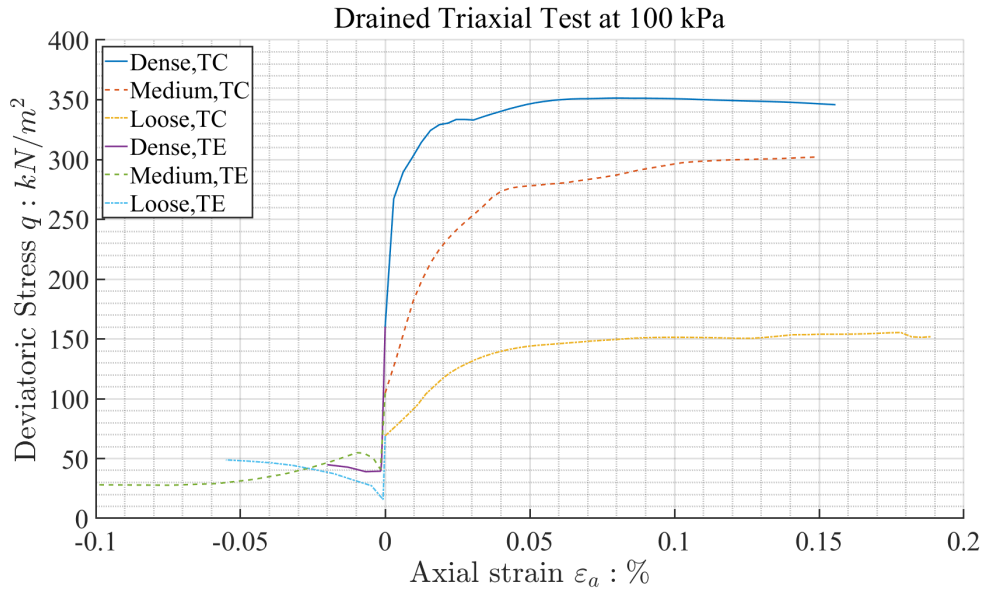


Figure 2.4: Result of Drained Triaxial test at 100 kPa

Result of Elemental Triaxial Test at 200 kPa

Triaxial test at radial stress of 200 kPa is simulated using one by one block of the finite element formulation with the EMC model.

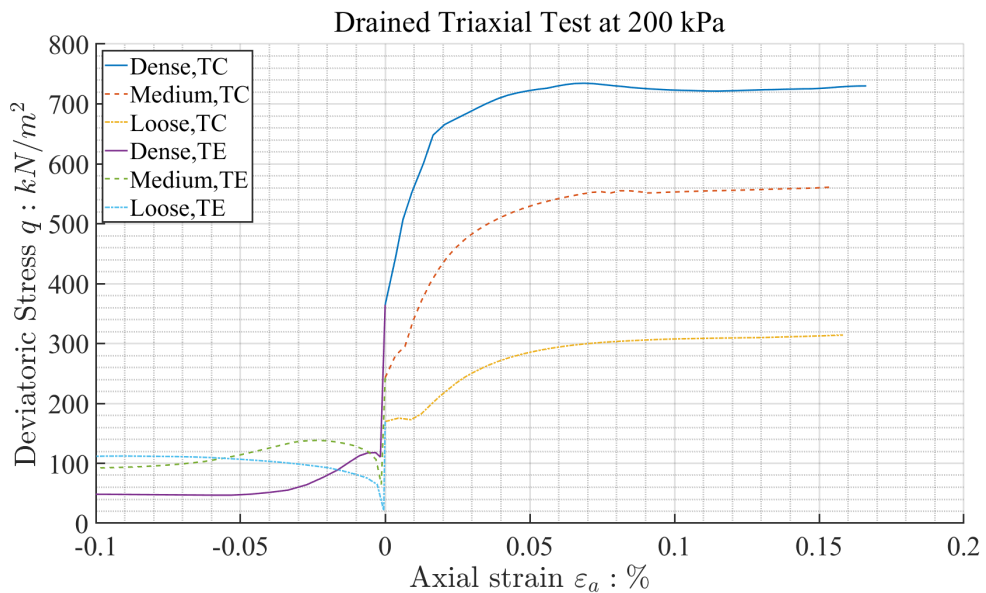


Figure 2.5: Result of Drained Triaxial test at 200 kPa

2. Calibration

2.2 Soil Parameters

2.2.1 Strain—Softening Stiffness—Hardening Model

Here is a table presenting the model parameters used by Sakai and Tanaka (1993).

Parameters	Loose	Medium	Dense
Density $\gamma(kN/m^3)$	13.5	14.8	16.3
Void ratio e	0.95	0.78	0.62
Relative density D_r	0.05	0.53	0.95
Coefficient of shear modulus, G_0	500	500	500
Poisson's ratio, ν	0.3	0.3	0.3
Peak friction angle, $\phi_p(^{\circ})$	33	38	45
Residual friction angle, $\phi_r(^{\circ})$	33	33	33
Dilation angle, $\psi(^{\circ})$	0	10	20
Shear band thickness, $S.B.(cm)$	0.3	0.3	0.3
Soil parameter, a	0.1	0.1	0.1
Soil parameter, b	0.8	0.4	0.1
Soil parameter, ε_d	0.3	0.3	0.3
Soil parameter, m	0.4	0.2	0.1
Soil parameter, β	0.1	0.1	0.1

Table 2.1: Model parameters used by Sakai and Tanaka, 1993

2.2.2 Nonassociated Flow Rule (NA)

Here is a table presenting the model parameters used in Nonassociated (NA) simulations.

2. Calibration

Parameter	Dense	Medium	Loose
$E(MPa)$	50	25	15
ν	0.3	0.25	0.2
$c(kPa)$	0	0	0
$\phi(^{\circ})$	40	35	30
$\psi(^{\circ})$	10	5	0
$\gamma_{dry}(kN/m^3)$	18	16	14
$\gamma_{sat}(kN/m^3)$	21	20	19
K_0	0.3572	0.4264	0.5

Table 2.2: Soil parameters used in nonassociated flow (NA) simulations

2.2.3 Extended Mohr—Coulomb Model (EMC)

Here is a table presenting the model parameters used in Extended Mohr-Coulomb (EMC) simulations.

Parameter	Dense	Medium	Loose
$E_{50}(MPa)$	50	25	13
$E_{ur}(MPa)$	150	75	39
ν_{ur}	0.4	0.35	0.3
$c(kPa)$	0	0	0
$\phi(^{\circ})$	41	37	27
$\psi(^{\circ})$	17	11	-4
$\gamma_{dry}(kN/m^3)$	18	16	14
$\gamma_{sat}(kN/m^3)$	21	20	19
K_0	0.3572	0.4264	0.5
$p_{ref}(kPa)$	100	100	100
Soil parameter, m	0.5	0.5	0.5

Table 2.3: Soil parameters used in Extended Mohr-Coulomb Model (EMC) simulations

2. Calibration

2.3 Convergence Criteria

2.3.1 Mesh Convergence

Here is a table presenting the result of mesh convergence test on both NA and EMC models.

The goal of the mesh convergence test usually is to seek the acceptable range of number of the mesh size. However, the interest in the present paper differs from the previously investigated objectives, in a way that the object sought is not the same. The present paper seeks to draw a more detailed analysis of the failure surface formed as the soil is sheared.

Some authors in the past described this with the width of the shear band (Tanaka and Sakai, 1993). However, the present paper deals only with the limit analysis formulation using the Extended Mohr-Coulomb model.

Type of Analysis	Mesh Number	$p_u, kN/m^2$	Variance	Std
Non-associated (NA)	250	137.7	0.11	0.33
Non-associated (NA)	500	135.8	1.23	1.11
Non-associated (NA)	1000	129.4	13.85	3.72
Non-associated (NA)	2000	139.8	0.28	0.52
Non-associated (NA)	5000	138.2	0.02	0.13
Non-associated (NA)	10000	141.7	1.69	1.30
Non-associated (NA)	20000	147	12.00	3.46
Exteded Mohr-Coulomb (EMC)	250	161.3	1.51	1.23
Exteded Mohr-Coulomb (EMC)	500	159.6	0.29	0.54
Exteded Mohr-Coulomb (EMC)	1000	161.4	1.62	1.27
Exteded Mohr-Coulomb (EMC)	2000	158.4	0.00	0.05
Exteded Mohr-Coulomb (EMC)	5000	157.3	0.16	0.40
Exteded Mohr-Coulomb (EMC)	10000	156.2	0.73	0.85
Exteded Mohr-Coulomb (EMC)	20000	153.8	3.35	1.83

Table 2.4: Setup and result of mesh convergence test

2. Calibration

Mesh Convergence Results

The result of the present investigation is the determination of the number of the mesh elements be around 2000.

However, it is noted that further studies, outside of this paper, is onto the maximum number of the elements to be studied, for this will enhance the visualization of the shear band formation, as well as the guidance onto the study of the shear dissipation.

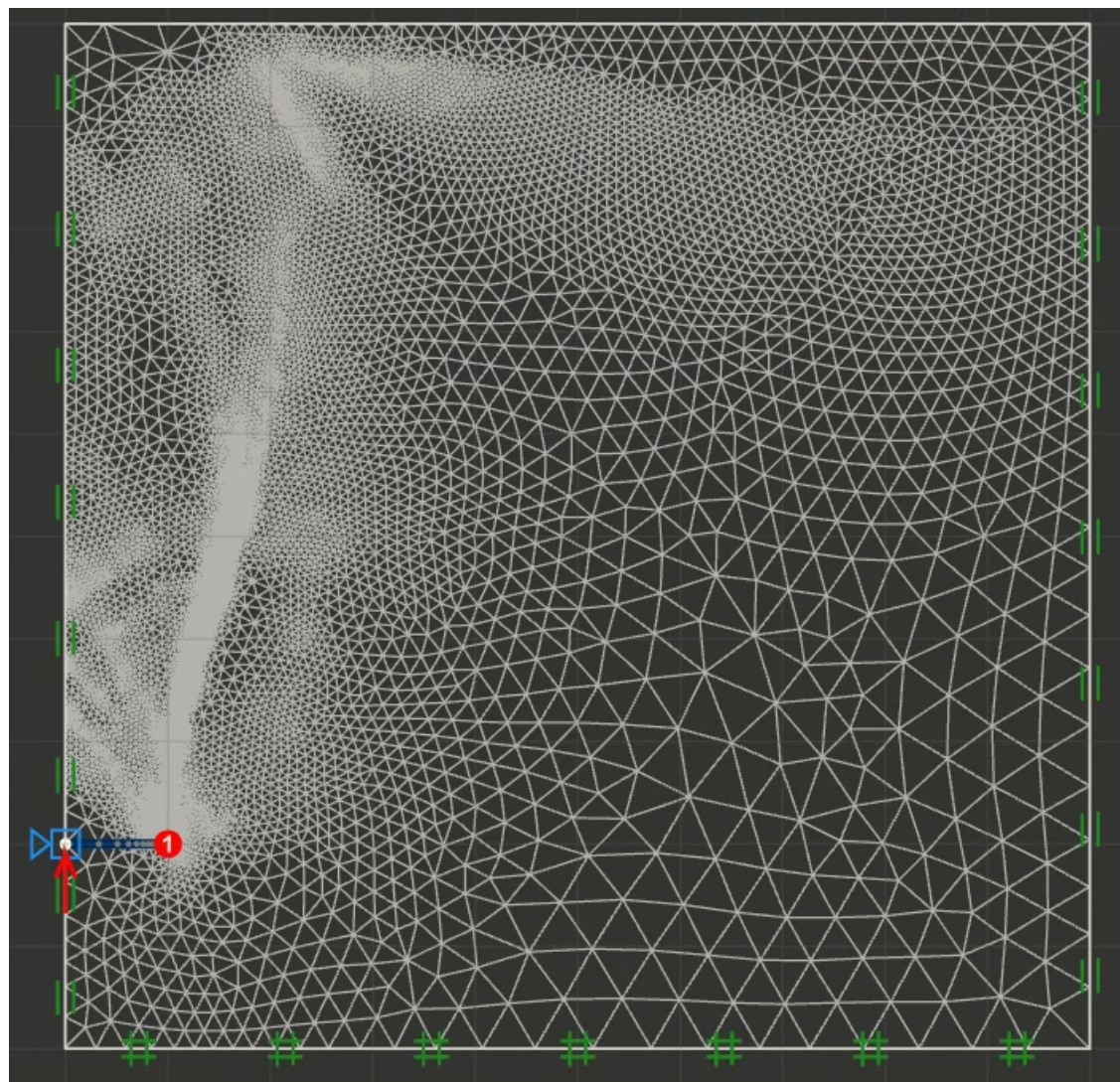


Figure 2.6: Typical result from mesh convergence test (maximum number of elements)

2. Calibration

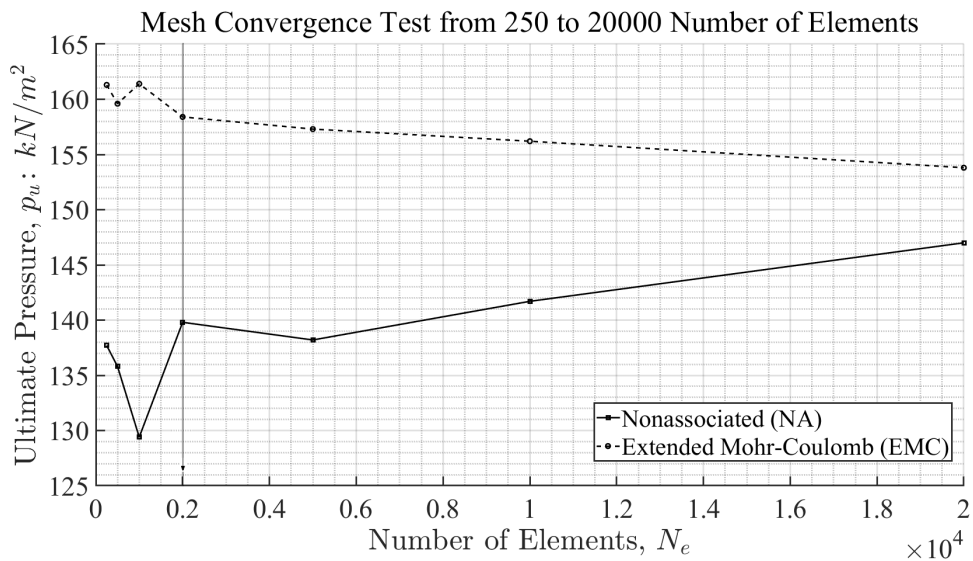


Figure 2.7: Result of the mesh convergence test, which confirms that about 2000 elements are acceptable

2. Calibration

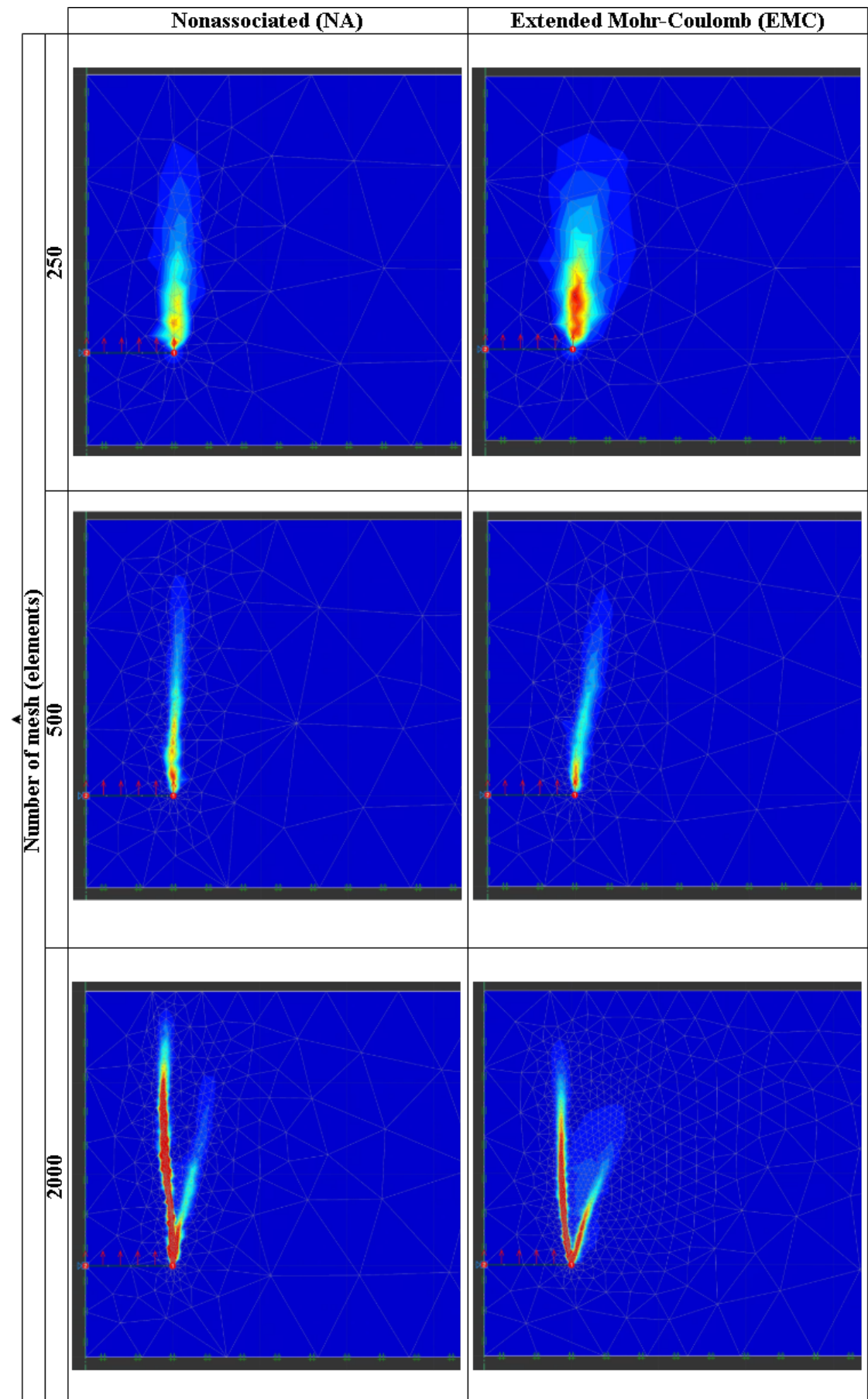


Figure 2.8: Shear Dissipation of the mesh convergence test of 250, 500, 2000 elements ²¹

2. Calibration

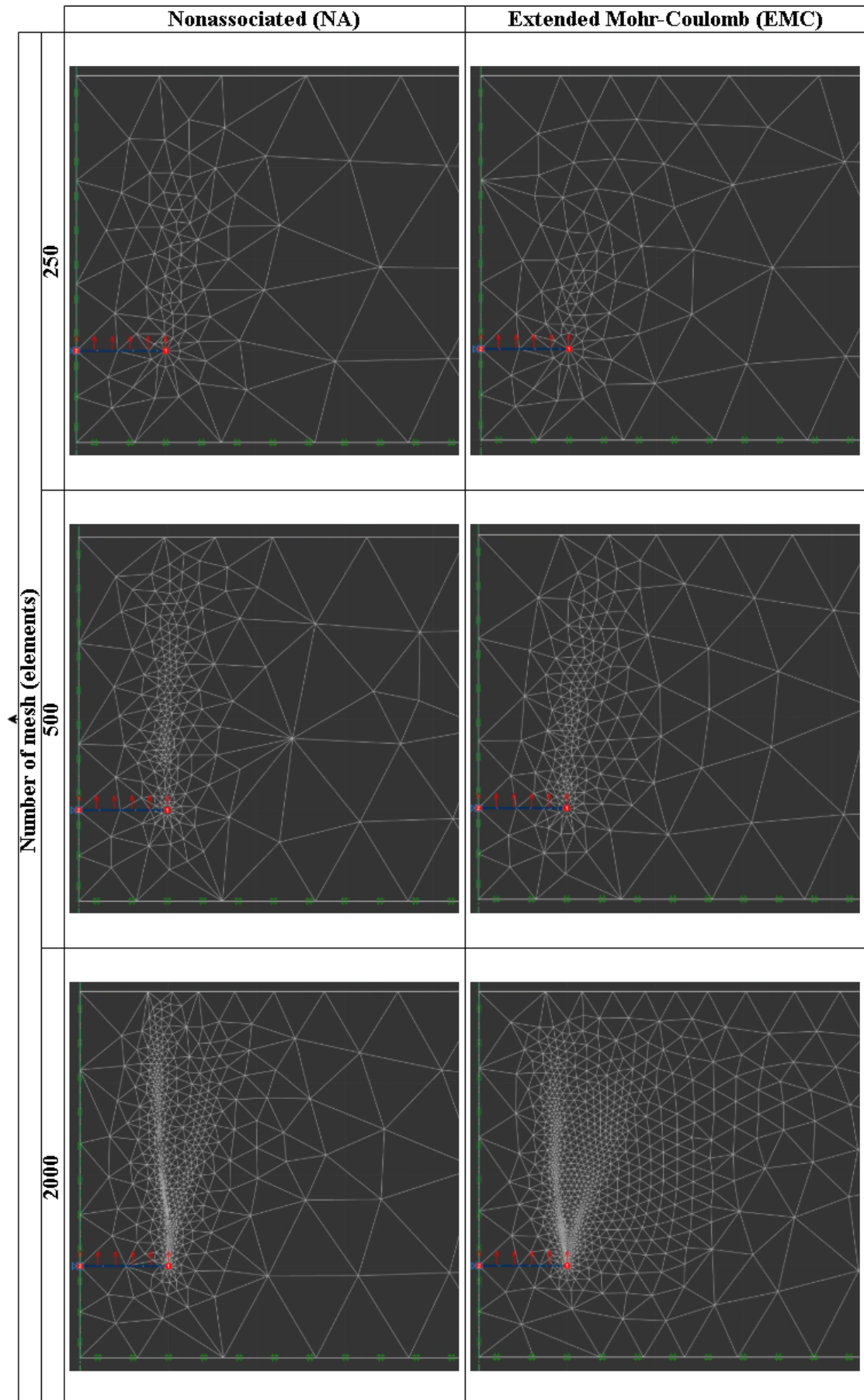


Figure 2.9: Mesh of 250, 500, 2000 elements

2. Calibration

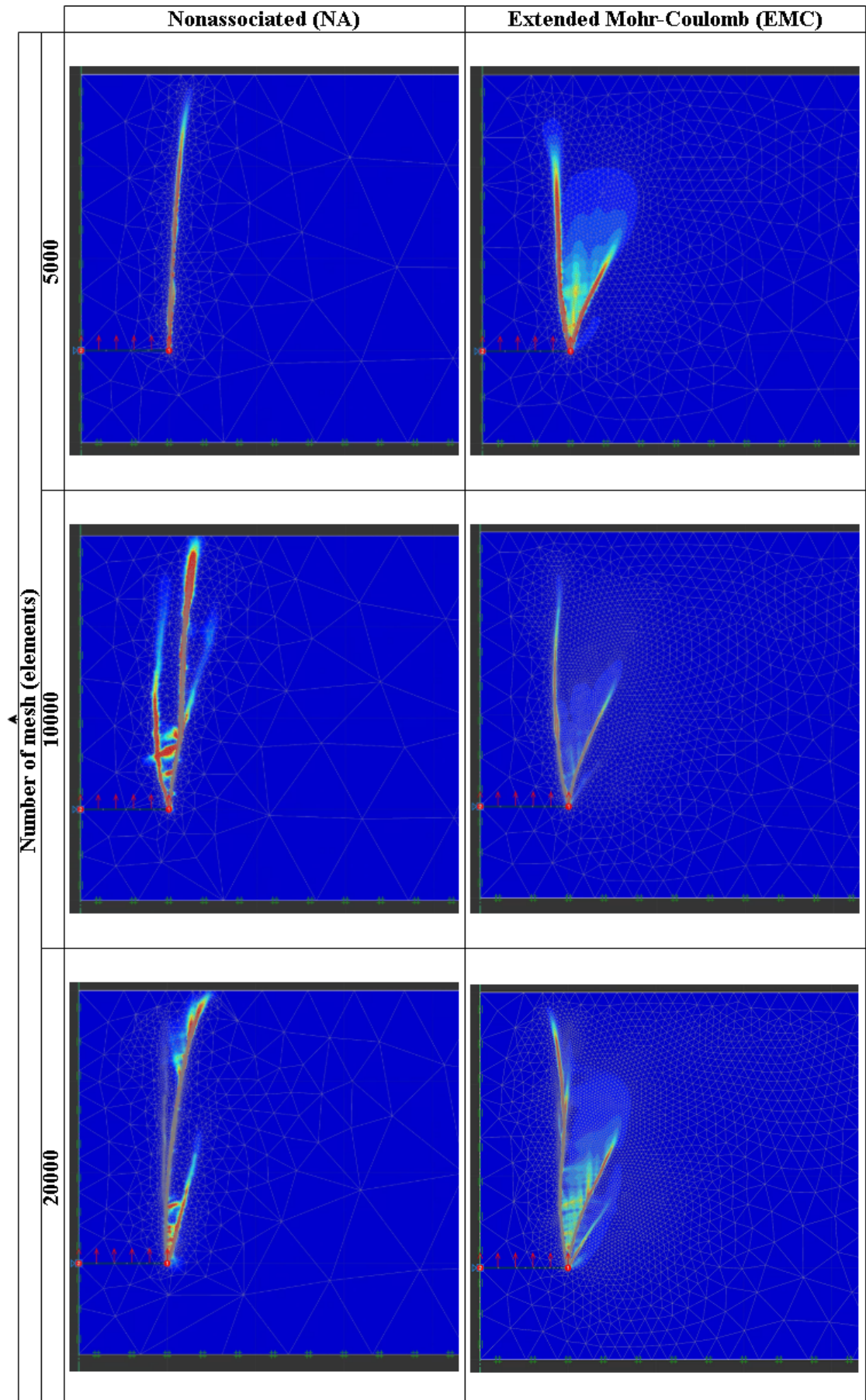


Figure 2.10: Shear Dissipation of the mesh convergence test of 5000, 10000, 20000²³ elements

2. Calibration

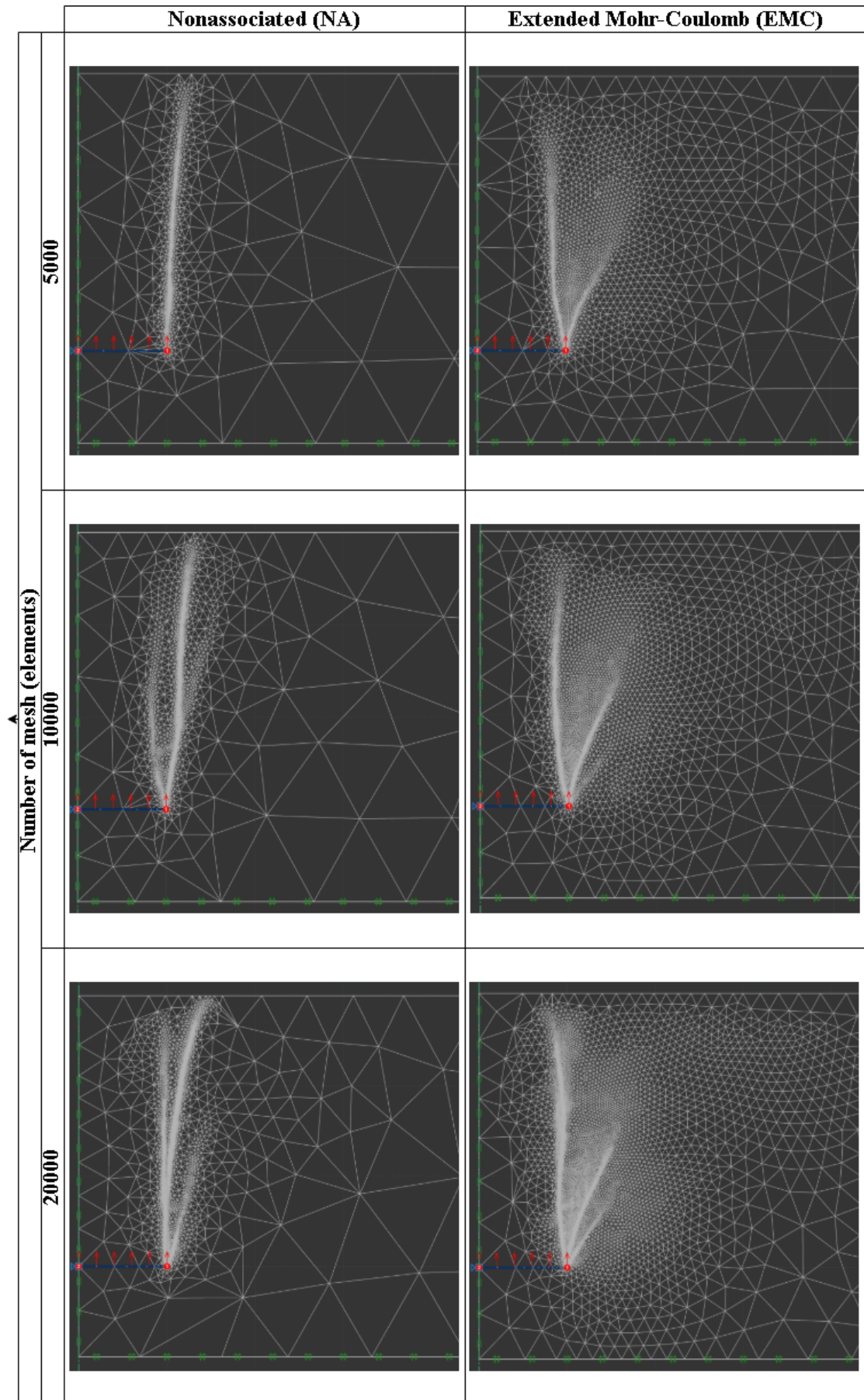


Figure 2.11: Mesh of 5000, 10000, 20000 elements

2. Calibration

2.3.2 Boundary Convergence

The soil tank width and the distance below the anchor to the soil tank boundary

are the primary concern for the modeling.

Therefore, the optimized value of the soil tank width has been investigated, by differing the values from 10B to 3B, , wherein B refers to the width of the anchor plate.

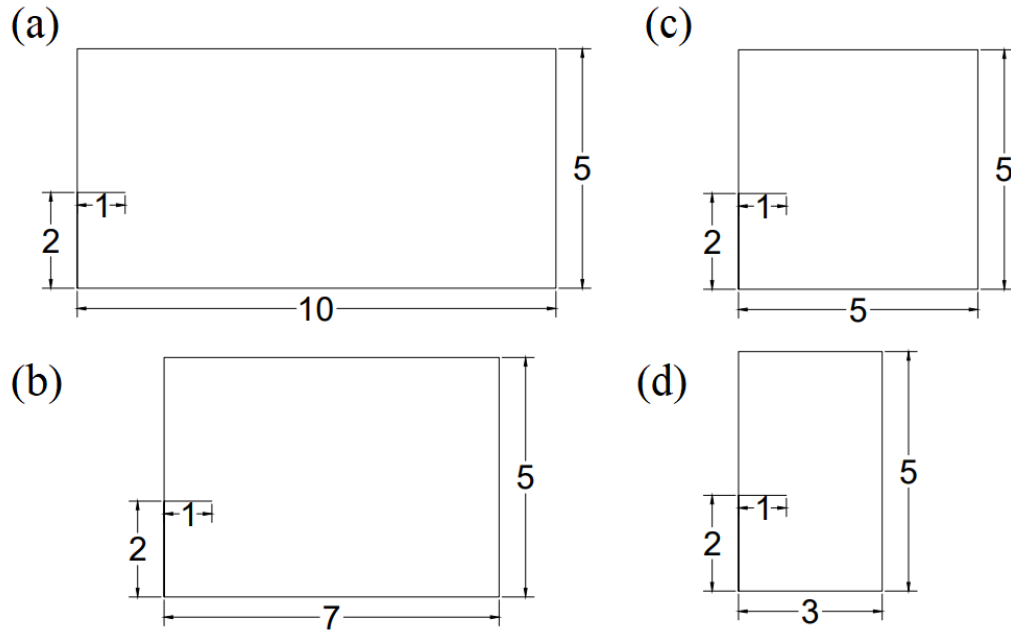


Figure 2.12: Convergence test setup on different boundary size: (a) 10B, (b) 7B, (c) 5B, (d) 3B

Due to the reasoning which considers the method of mesh adaptivity, insignificant effect onto the extension of the soil tank width has been deemed acceptable by the author. Therefore, the result of the boundary convergence test is determined at 10B.

2. Calibration

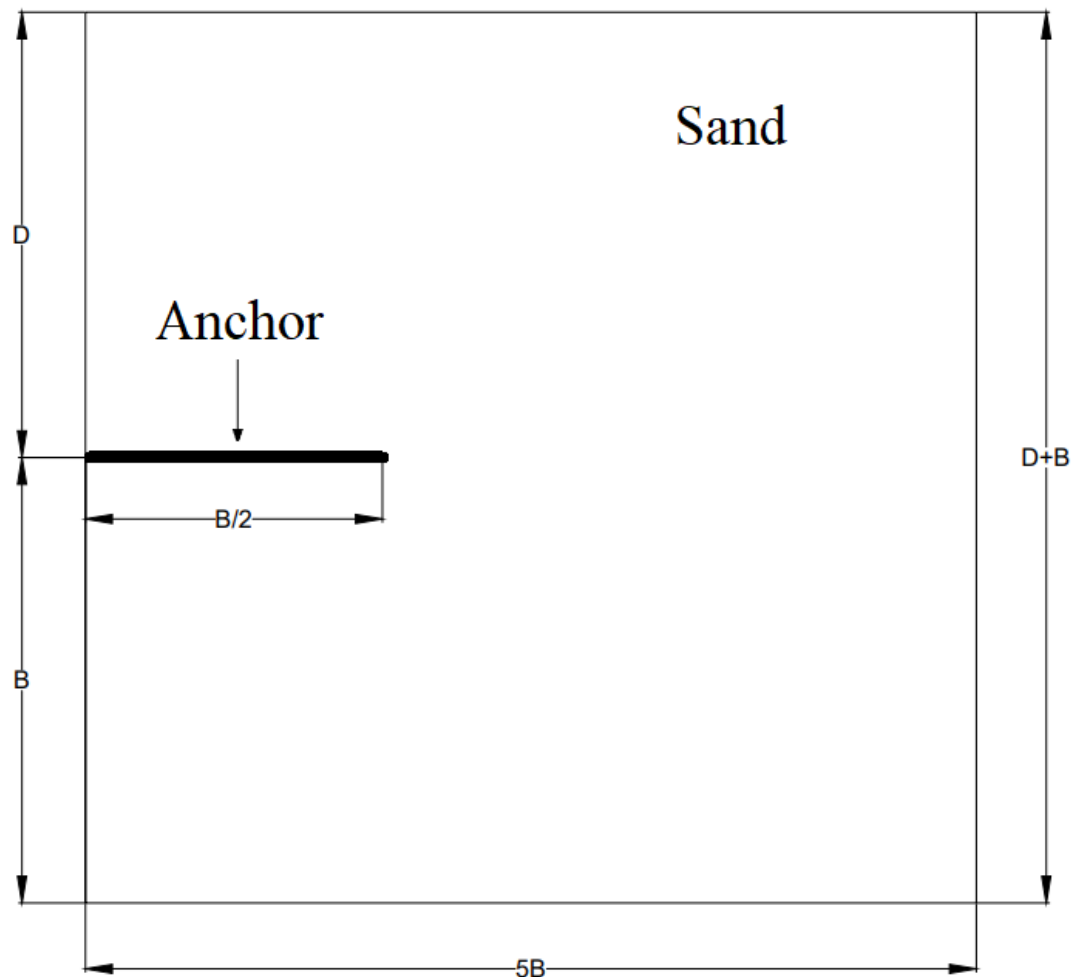


Figure 2.13: Final boundary decision schematic for numerical simulations

Here is a table presenting the setup of boundary convergence test on both NA and EMC models.

2. Calibration

Width Boundary	Depth Below Anchor	D/B	Soil Type	Test Type
10B	2B	3	Dense	NA, EMC
7B	2B	3	Dense	NA, EMC
5B	2B	3	Dense	NA, EMC
3B	2B	3	Dense	NA, EMC
10B	2B	3	Medium	NA, EMC
7B	2B	3	Medium	NA, EMC
5B	2B	3	Medium	NA, EMC
3B	2B	3	Medium	NA, EMC
10B	2B	3	Loose	NA, EMC
7B	2B	3	Loose	NA, EMC
5B	2B	3	Loose	NA, EMC
3B	2B	3	Loose	NA, EMC

Table 2.5: Setup of boundary convergence test

Boundary Convergence Results

3

Results

Contents

3.1 Parametric Study	28
3.1.1 Effect of Embedment Depth Ratio $\frac{D}{B}$	31
3.1.2 Effect of Width B	32
3.1.3 Shear Dissipation	32
3.2 Comparison with Previous Researchers	39

3.1 Parametric Study

Here is a table presenting the setup of the numerical simulations on both NA and EMC models.

The code refers to the differing width of the plate anchor, , whereas the number specifies if its embedment ratio is either 1, 2, or 3.

3. Result

Table 3.1: Setup for numerical simulations

Code	Test No.	Density	B, mm	D, mm	D/B
A	LA1	Loose	40	40	1
B	LB1	Loose	200	200	1
C	LC1	Loose	1000	1000	1
D	LD1	Loose	3500	3500	1
E	LE1	Loose	4500	4500	1
G	LG1	Loose	6500	6500	1
A	MA1	Medium	40	40	1
B	MB1	Medium	200	200	1
C	MC1	Medium	1000	1000	1
D	MD1	Medium	3500	3500	1
E	ME1	Medium	4500	4500	1
G	MG1	Medium	6500	6500	1
A	DA1	Dense	40	40	1
B	DB1	Dense	200	200	1
C	DC1	Dense	1000	1000	1
D	DD1	Dense	3500	3500	1
E	DE1	Dense	4500	4500	1
G	DG1	Dense	6500	6500	1
A	LA2	Loose	40	80	2
B	LB2	Loose	200	400	2
C	LC2	Loose	1000	2000	2
D	LD2	Loose	3500	7000	2
E	LE2	Loose	4500	9000	2
G	LG2	Loose	6500	13000	2
A	MA2	Medium	40	80	2
B	MB2	Medium	200	400	2
C	MC2	Medium	1000	2000	2
D	MD2	Medium	3500	7000	2
E	ME2	Medium	4500	9000	2
G	MG2	Medium	6500	13000	2

3. Result

Table 3.1 continued from previous page

Code	Test No.	Density	B, mm	D, mm	D/B
A	DA2	Dense	40	80	2
B	DB2	Dense	200	400	2
C	DC2	Dense	1000	2000	2
D	DD2	Dense	3500	7000	2
E	DE2	Dense	4500	9000	2
G	DG2	Dense	6500	13000	2
A	LA3	Loose	40	120	3
B	LB3	Loose	200	600	3
C	LC3	Loose	1000	3000	3
D	LD3	Loose	3500	10500	3
E	LE3	Loose	4500	13500	3
G	LG3	Loose	6500	19500	3
A	MA3	Medium	40	120	3
B	MB3	Medium	200	600	3
C	MC3	Medium	1000	3000	3
D	MD3	Medium	3500	10500	3
E	ME3	Medium	4500	13500	3
G	MG3	Medium	6500	19500	3
A	DA3	Dense	40	120	3
B	DB3	Dense	200	600	3
C	DC3	Dense	1000	3000	3
D	DD3	Dense	3500	10500	3
E	DE3	Dense	4500	13500	3
G	DG3	Dense	6500	19500	3

3. Result

3.1.1 Effect of Embedment Depth Ratio $\frac{D}{B}$

Overall Results with All Range of Dense, Medium, Loose Sands

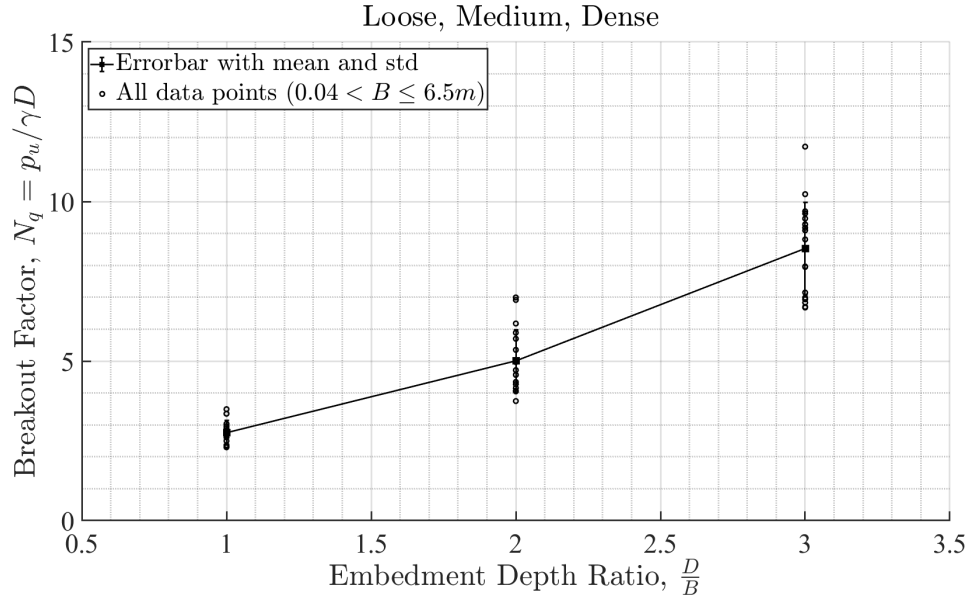


Figure 3.1: Effect of embedment depth ratio on break-out factor for all densities of soil

For Different Sand Densities: *Loose, Medium, Dense*

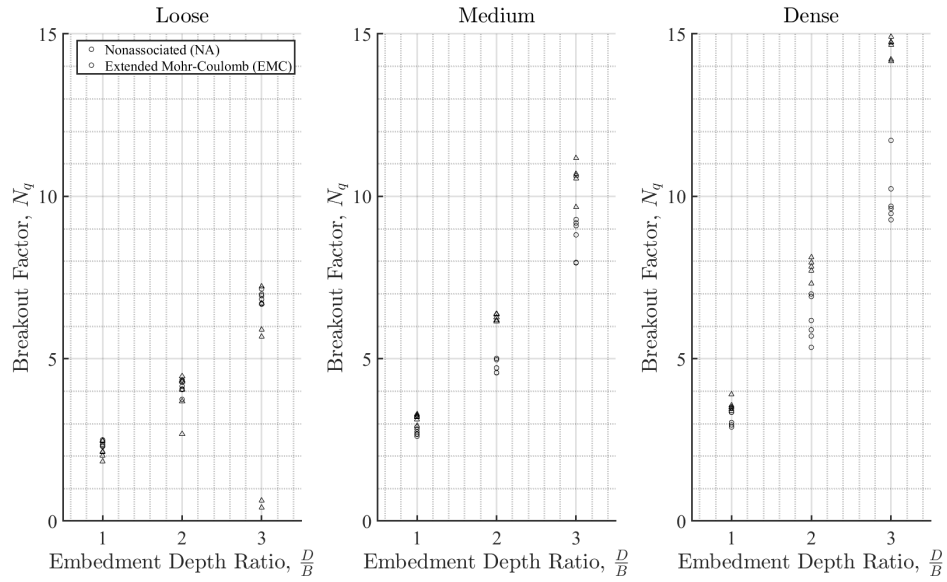


Figure 3.2: Effect of embedment depth ratio on break-out factor (a) loose (b) medium (c) dense

3. Result

3.1.2 Effect of Width B

Overall Results with All Range of Dense, Medium, Loose Sands

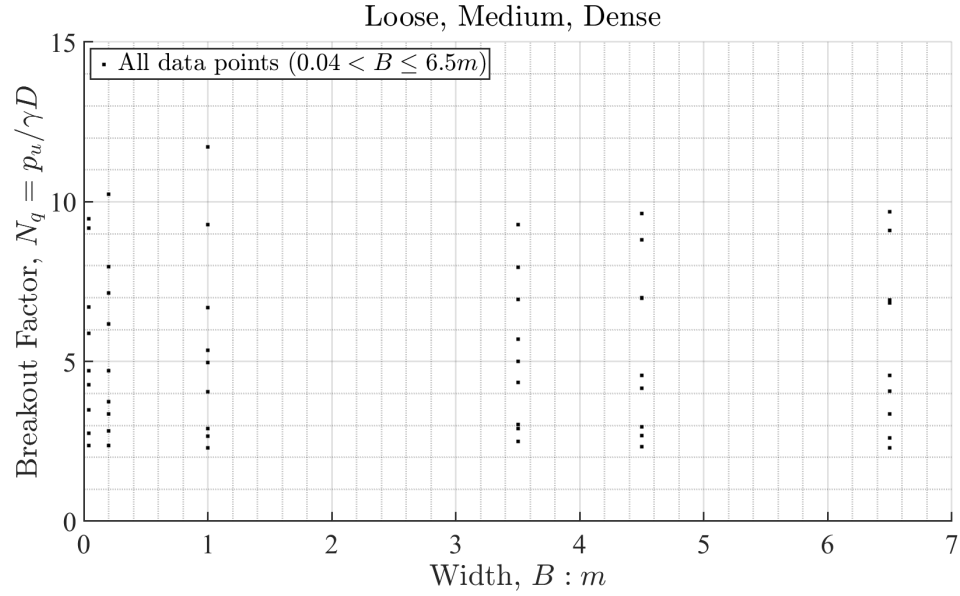


Figure 3.3: Effect of width of plate for all densities of soil

3.1.3 Shear Dissipation

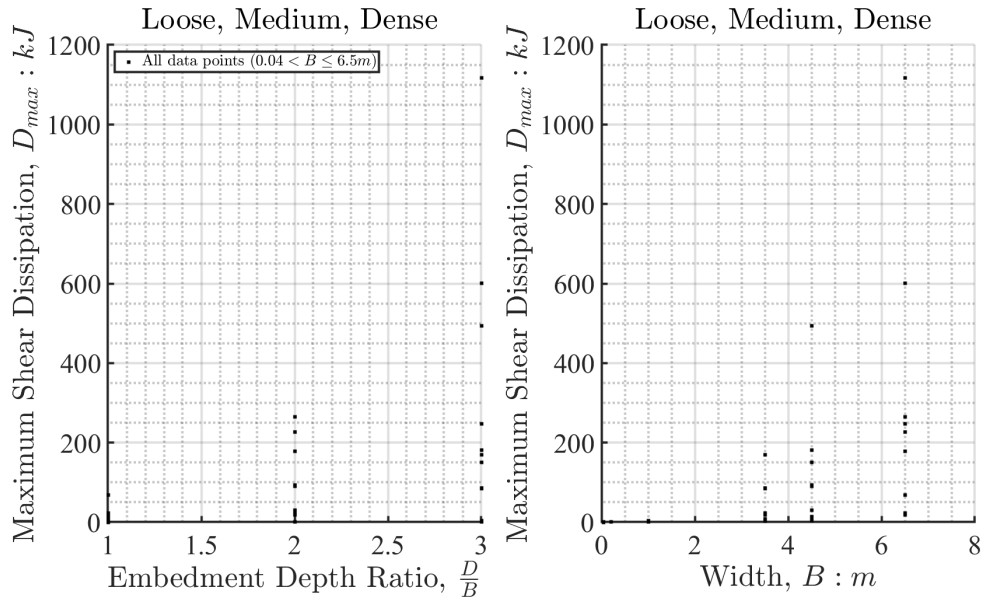


Figure 3.4: Effect of embedment depth and width on shear dissipation for all densities of soil

3. Result

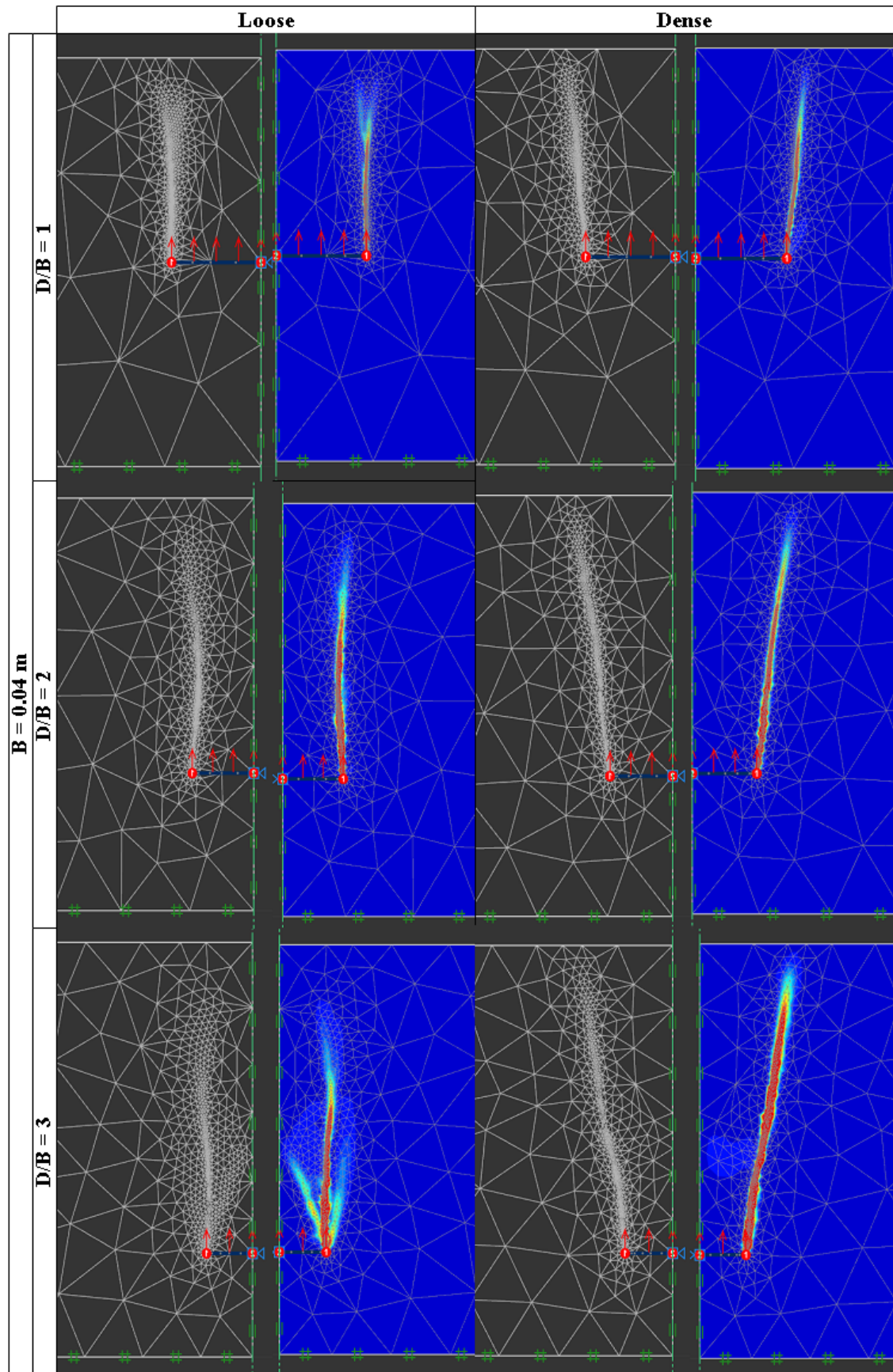


Figure 3.5: Shear dissipation of NA model at 10 percent of the maximum value and $B = 0.04m$

3. Result

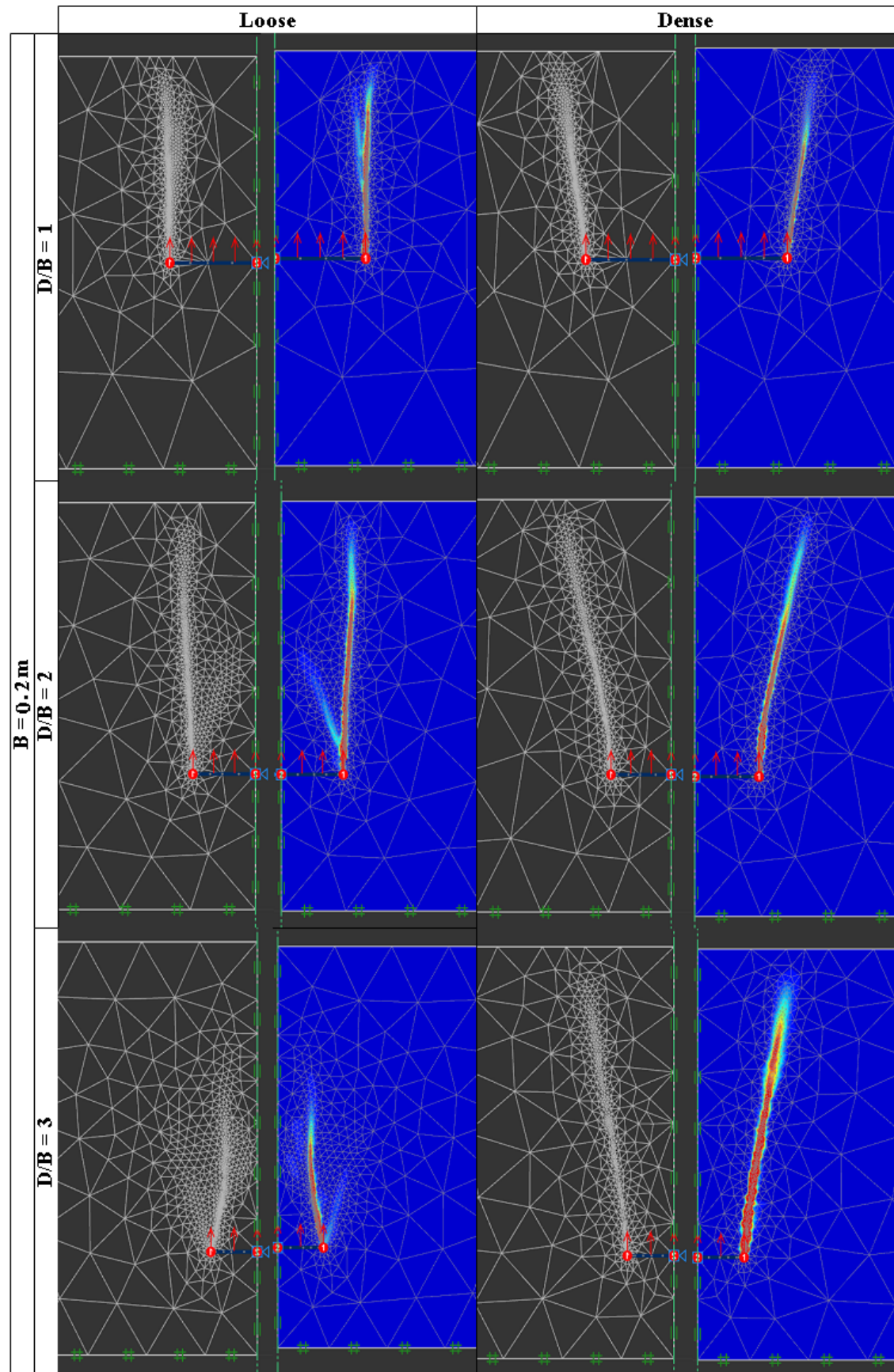


Figure 3.6: Shear dissipation of NA model at 10 percent of the maximum value and $B = 0.2m$

3. Result

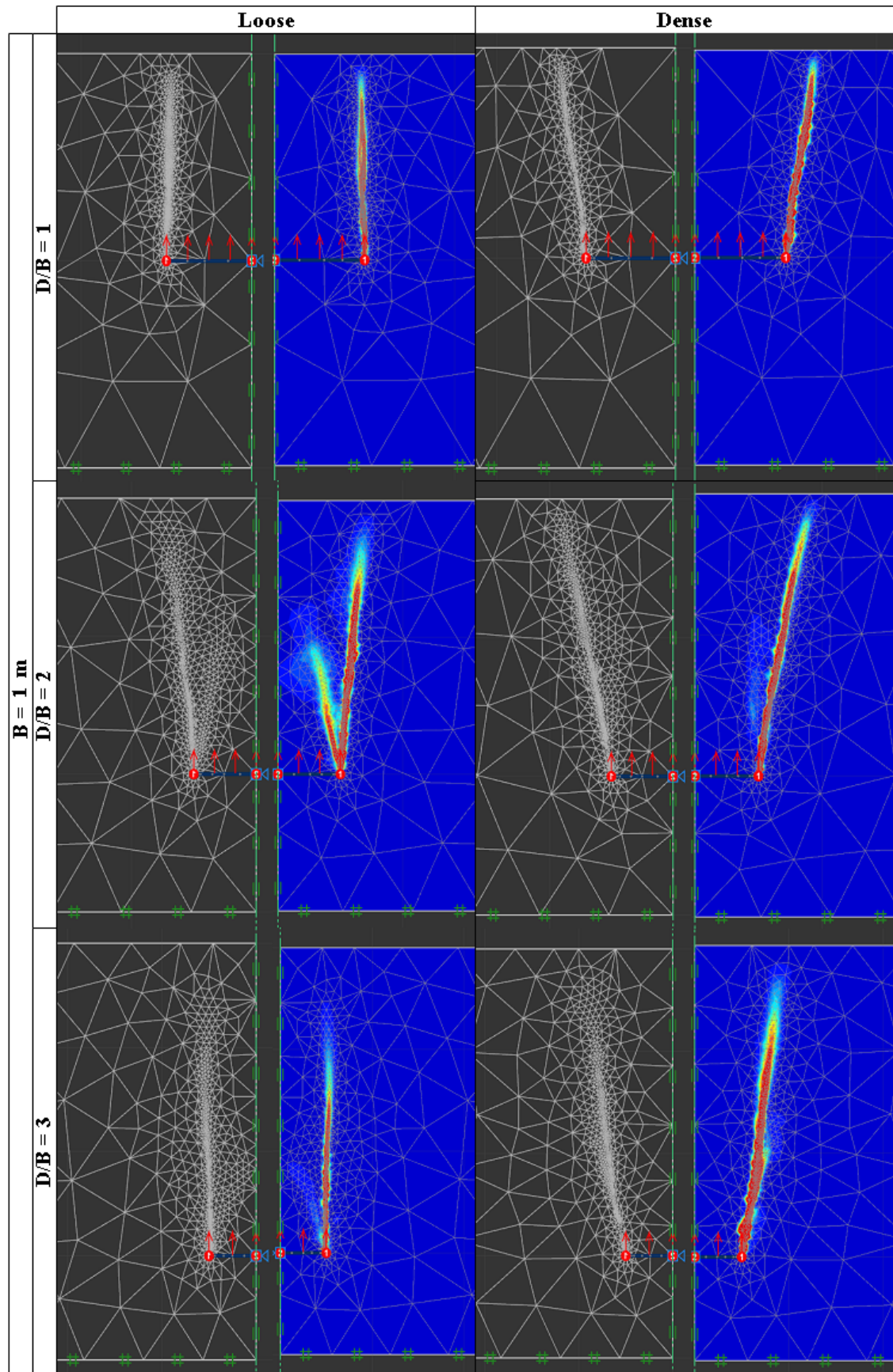


Figure 3.7: Shear dissipation of NA model at 10 percent of the maximum value and $B = 1.0m$

3. Result

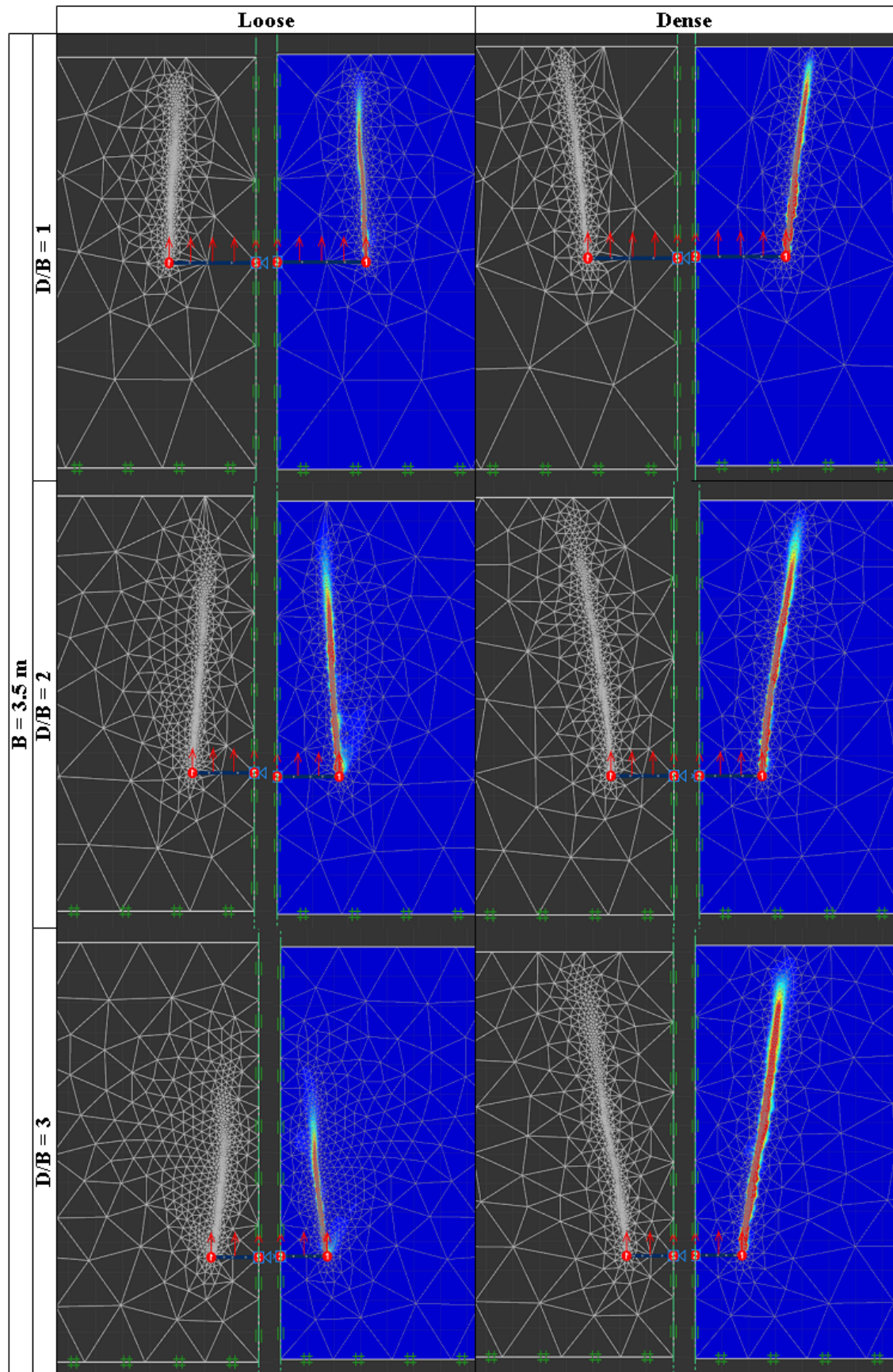


Figure 3.8: Shear dissipation of NA model at 10 percent of the maximum value and $B = 3.5\text{m}$

3. Result

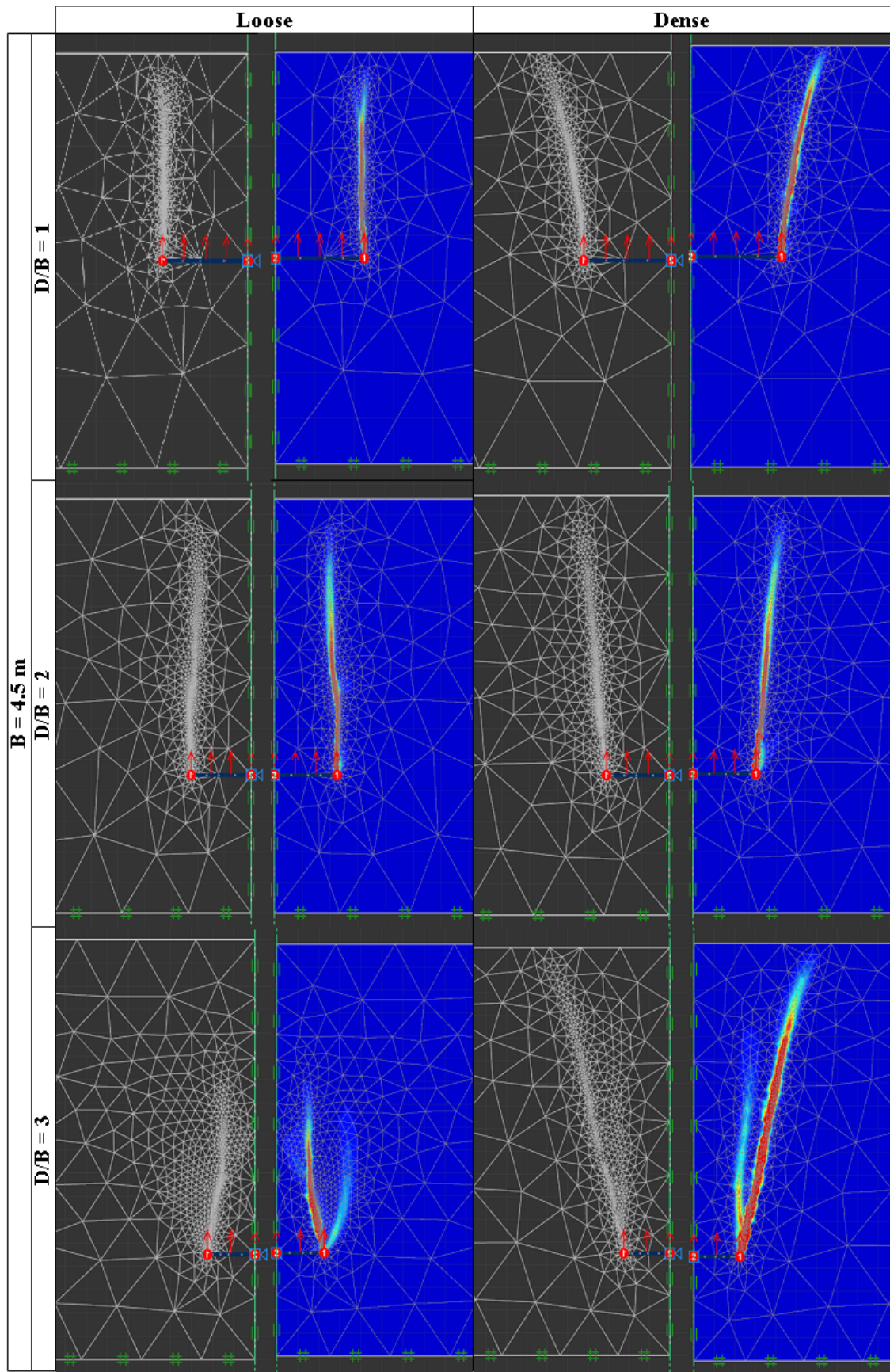


Figure 3.9: Shear dissipation of NA model at 10 percent of the maximum value and $B = 4.5\text{m}$

3. Result

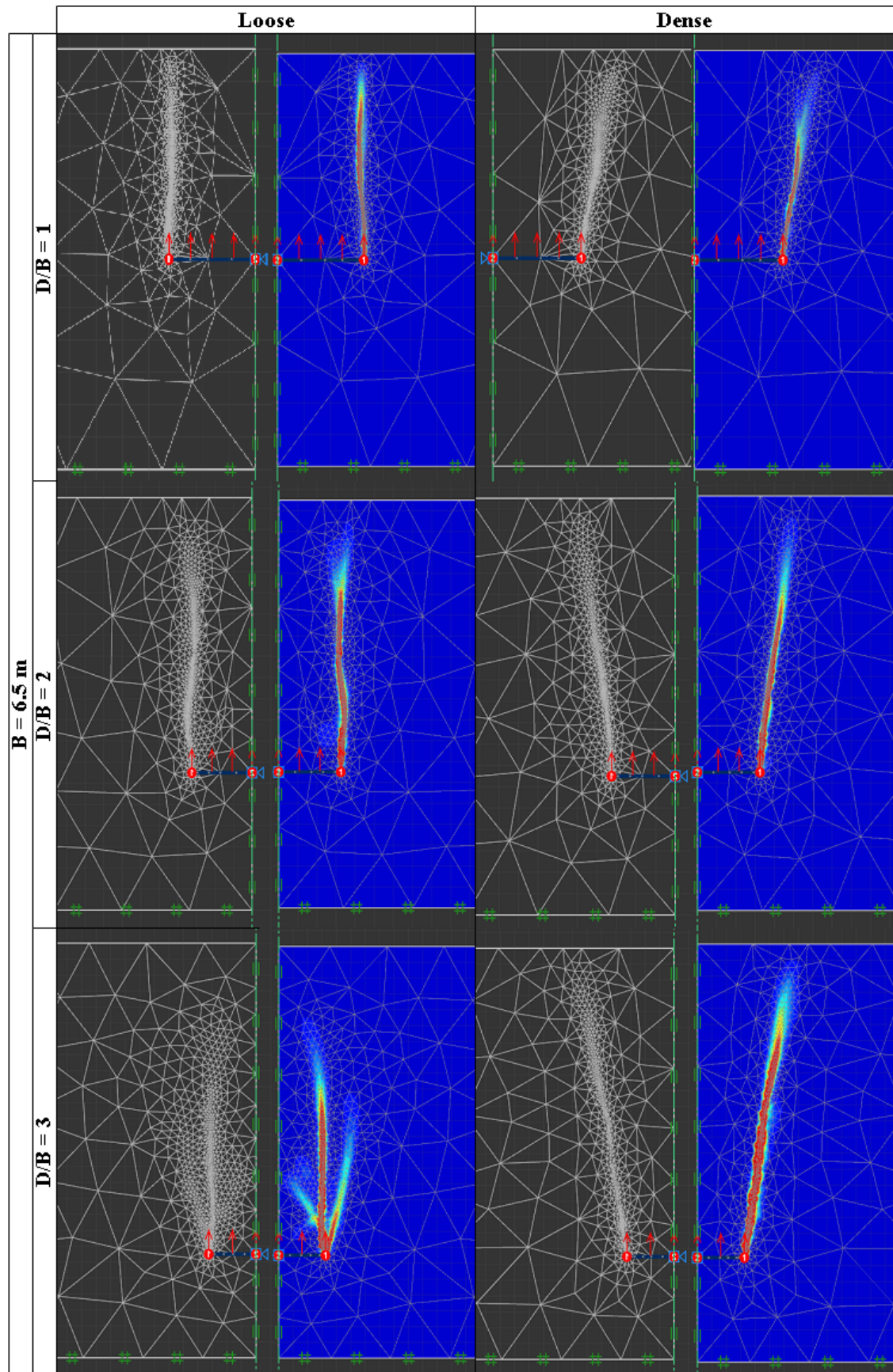


Figure 3.10: Shear dissipation of NA model at 10 percent of the maximum value and $B = 6.5\text{m}$

3. Result

3.2 Comparison with Previous Researchers

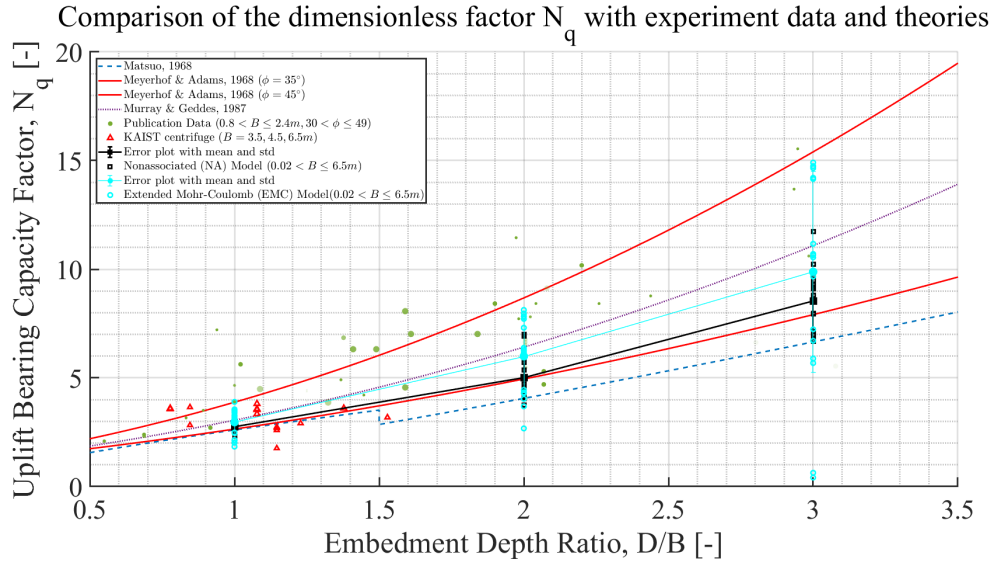


Figure 3.11: Comparison with theories and experimental data in all densities of sands

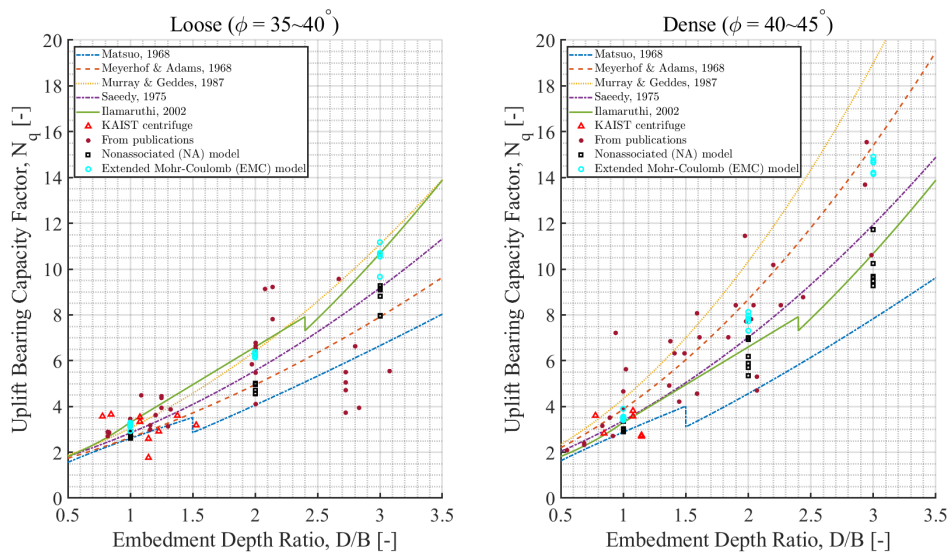


Figure 3.12: Comparison with theories and experimental data in loose and dense sands

3. Result

Comparison of the plot of the effect of width on resistance

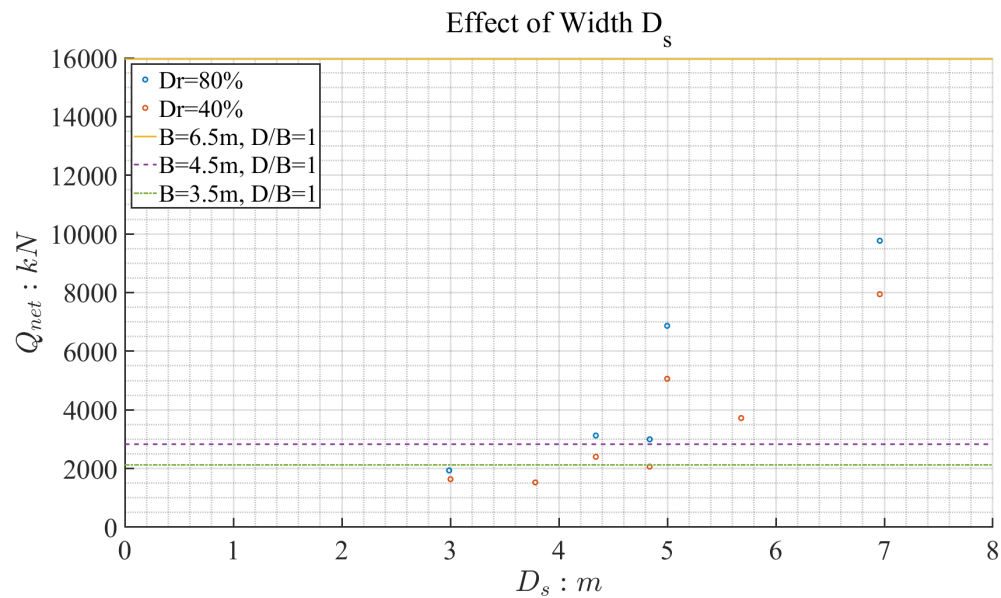


Figure 3.13: Comparison drawn

4

Comparison with Centrifuge Experiment

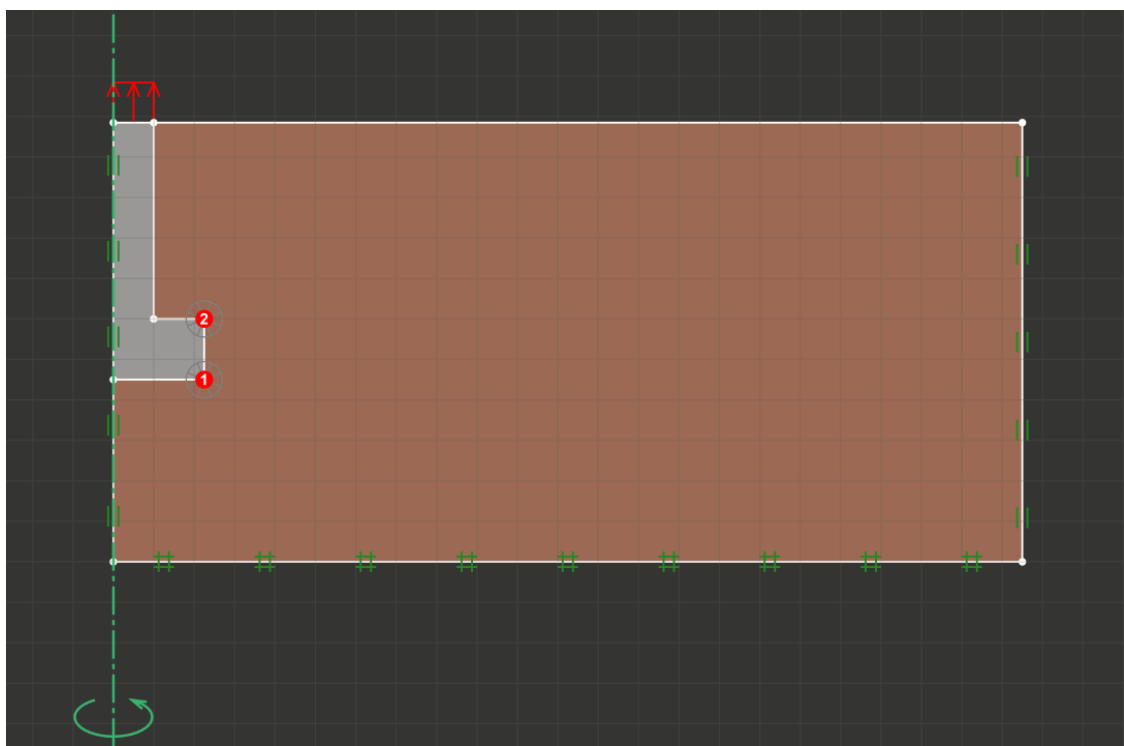


Figure 4.1: Typical numerical test set-up

4. Comparison with Centrifuge Experiment

The goal is to find the best matching load—displacement curve by comparing the measurements with the models: EMC and NA.

In order to find the suitable pair of a set of variables, the values were varied by interpolating those in between the dense and the loose sands of the representative values from the example file provided by the software. The result is that for the EMC model, the set named B and C show a good match, whereas for the NA model, the set with H and G display a favorable fit. The chosen set of parameters are presented in the tables below:

Table 4.1: Set of varied model parameters of EMC model

EMC					
Set	A	B	C	D	E
$E_{50}(MPa)$	25	20	22.5	35	40
$E_{ur}(MPa)$	75	60	67.5	105	120
ν_{ur}	0.3	0.3	0.3	0.3	0.3
$c(kPa)$	0	0	0	0	0
$\phi(deg)$	37	34	35.5	38	40
$\psi(deg)$	11	1	5	8	14
$\gamma_d(kN/m^3)$	16	15.5	15.75	16.5	17
$\gamma_{sat}(kN/m^3)$	20	19	19.5	20.5	21
K_0	0.4264	0.4264	0.4264	0.4264	0.4264
$p_{ref}(kPa)$	100	100	100	100	100
m	0.5	0.5	0.5	0.5	0.5

Table 4.2: Set of varied model parameters for NA model

NA					
Set	F	G	H	I	J
$E(MPa)$	25	20	30	35	40
ν	0.25	0.25	0.25	0.25	0.25

4. Comparison with Centrifuge Experiment

Table 4.2 continued from previous page

NA					
$c(kPa)$	0	0	0	0	0
$\phi(deg)$	35	33	37	39	41
$\psi(deg)$	5	4	6	7	8
$\gamma_d(kN/m^3)$	16	14	15	16	14
$\gamma_{sat}(kN/m^3)$	20	19	19.5	20	19
K_0	0.4264	0.4264	0.4264	0.4264	0.4264

The table below show the KAIST centrifuge test set-up and the results.

Table 4.3: Centrifuge test set-up and result

Case	$B(m)$	$\frac{D}{B}$	$\gamma_d(kN/m^3)$	$Q_u(kN)$
1-1	4.5	1	13.8	2959
1-2	4.5	1.3	13.8	3845
1-3	4.5	1.3	13.8	4050
2-1	6.5	1	14	7433
2-2	6.5	1.3	14	10440
2-3	6.5	1.3	14	10590
3-1	4.5	1	15.3	3312
3-2	4.5	1.3	15.3	4554
3-3	4.5	1.3	15.3	4824
4-1	6.5	1	15.3	9331
4-2A	6.5	1.3	15.3	12280
4-3	6.5	1.3	15.3	12240
5-1	3.5	1.3	14	1980
5-2	3.5	1.6	14	2658
5-3	4.5	1.6	14	5351
6-3	3.5	1.6	15.1	3616

The table 4.4 shows the numerical test set-up, mainly for the dimensions corresponding the formulated in-house codes.

4. Comparison with Centrifuge Experiment

Table 4.4: Numerical model set-up for load-displacement curve comparison

Code	$B(m)$	$D - t(m)$	$D(m)$	$t(m)$	$b(m)$	$A(m^2)$
base2	6.5	5.95	7.45	1.5	1	39.1
base3	6.5	4	5.5	1.5	1	39.1
base2	6.5	5.95	7.45	1.5	1	39.1
base3	6.5	4	5.5	1.5	1	39.1
base2	6.5	5.95	7.45	1.5	1	39.1
base2	6.5	5.95	7.45	1.5	1	39.1
base2	6.5	5.95	7.45	1.5	1	39.1
base2	6.5	5.95	7.45	1.5	1	39.1
base6	4.5	2	3.5	1.5	1	17.1
base5	4.5	3.35	4.85	1.5	1	17.1
base5	4.5	3.35	4.85	1.5	1	17.1
base6	4.5	2	3.5	1.5	1	17.1
base5	4.5	3.35	4.85	1.5	1	17.1
base5	4.5	3.35	4.85	1.5	1	17.1
base4	4.5	4.7	6.2	1.5	1	17.1
base8	3.5	3.55	4.3	0.75	0.6	11.1
base7	3.5	4.6	5.35	0.75	0.6	11.1

4. Comparison with Centrifuge Experiment

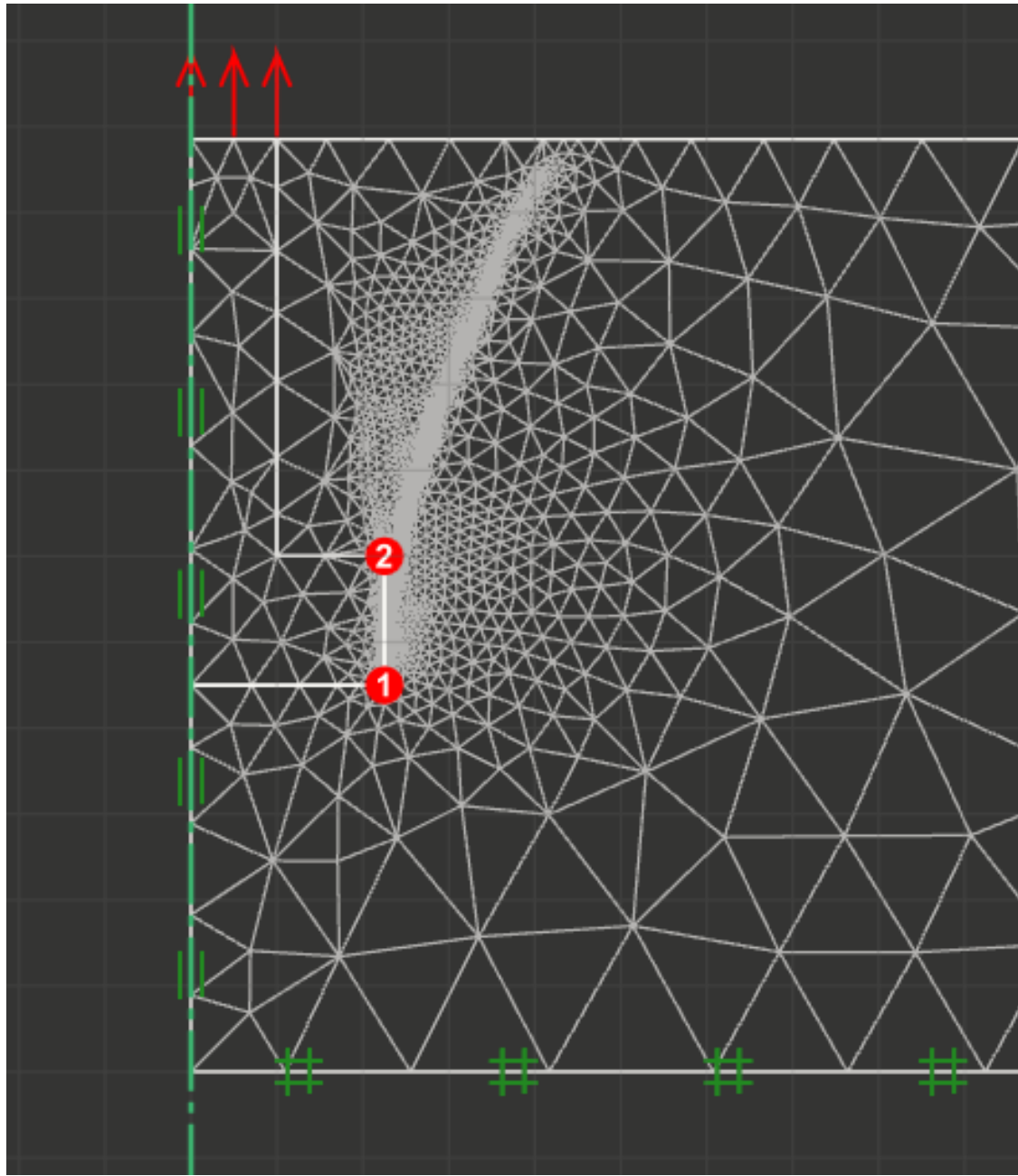


Figure 4.2: Typical mesh of the numerical simulation; number of mesh = 5000

While the mesh convergence test on the plate anchor pull-out test showed that the number of mesh around 2000 are reasonable, the final mesh number was chosen to be 5000 for more detailed representation of the shear dissipation bands in the graphics.

4. Comparison with Centrifuge Experiment

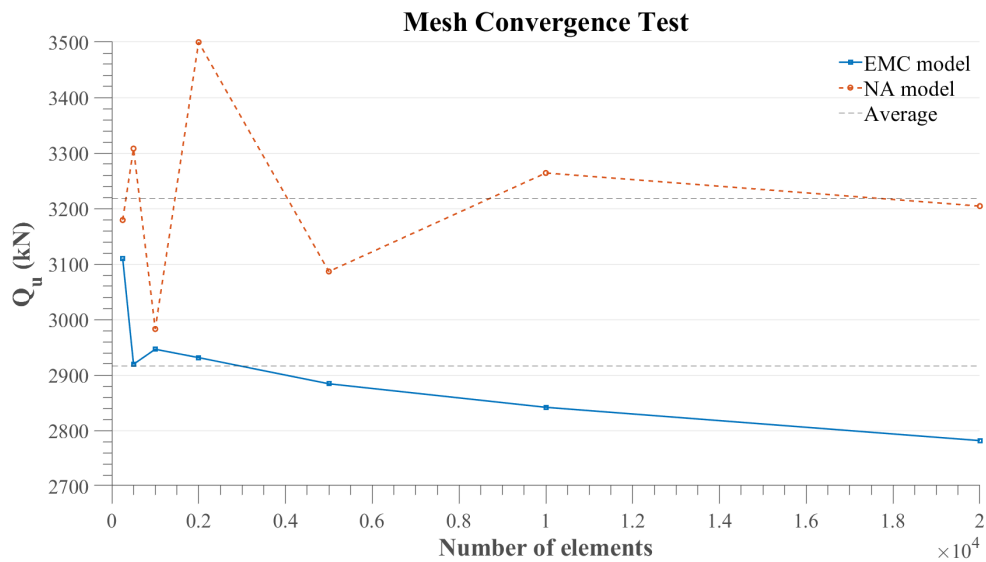


Figure 4.3: Mesh convergence test for numerical simulations on the shallow foundations using two models: EMC and NA

4. Comparison with Centrifuge Experiment

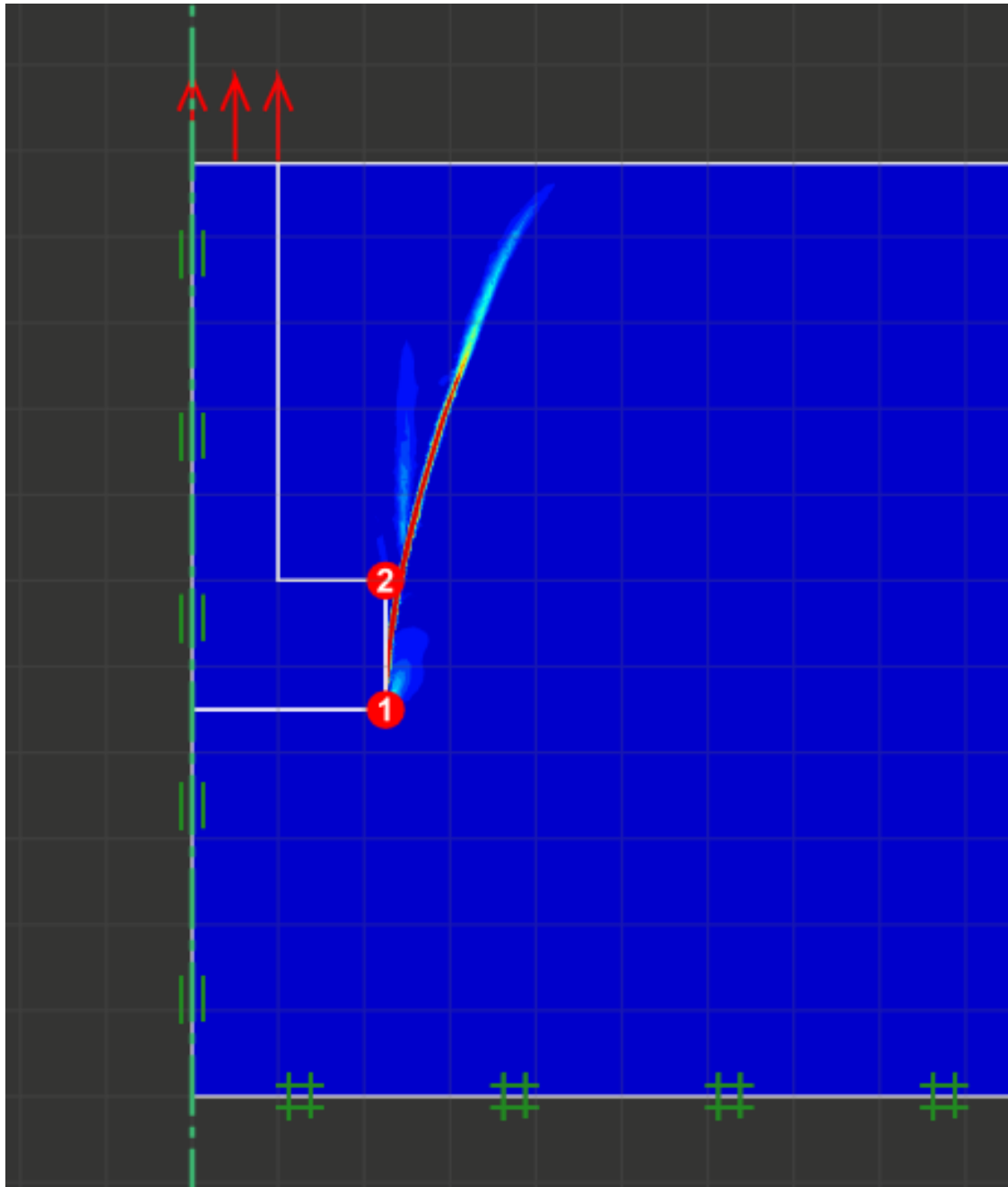


Figure 4.4: Typical result of the numerical simulation; 1st decile of the shear dissipation (kJ)

Results of numerical analysis for finding the model that fits the centrifuge load—displacement curve

The following load—displacement curves were generated by varying not only the codes but also the model parameters. The data from total number of 80 simulations

4. Comparison with Centrifuge Experiment

were accumulated to draw 8 plots with base numbers from 2 to 8, which represent the variation of the size of the footing width. In the plot below, the line with markers represent the NA model, whereas only those of the colored lines are the EMC models. It is noted that among 80 load—displacement curves, only 4 were selected for matching the dense and loose sand cases of the centrifuge test results.

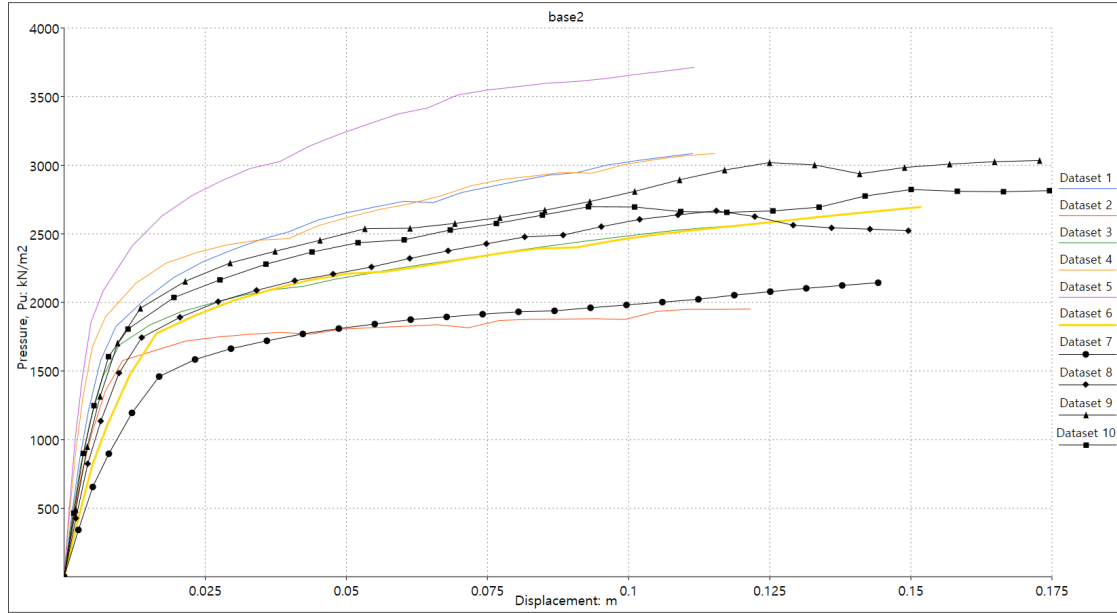


Figure 4.5: Code name base2; $B=6.5\text{m}$; $B/D = 0.915$

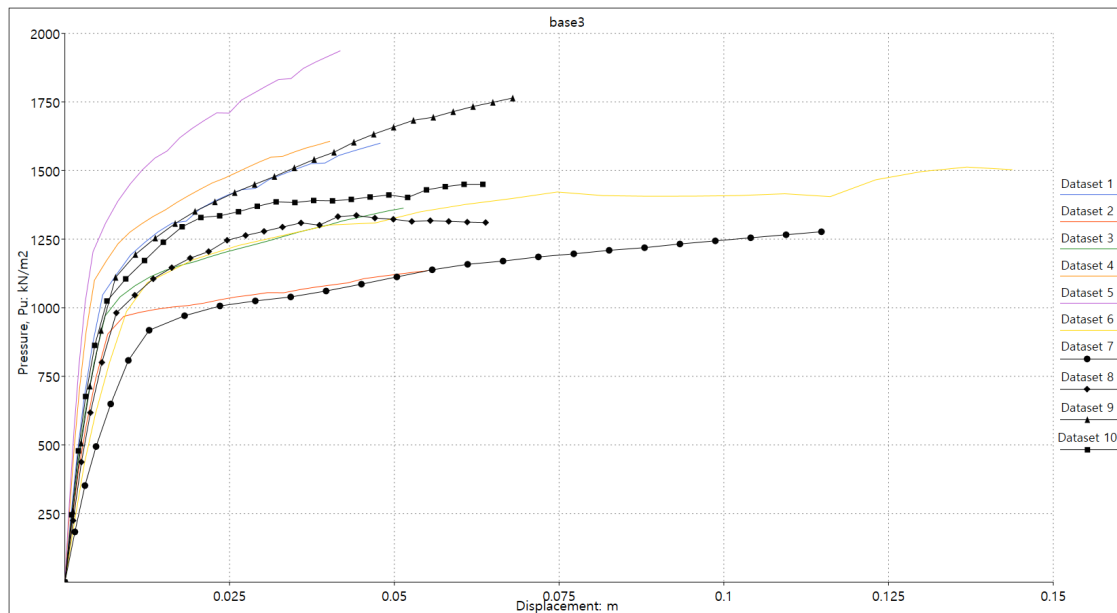


Figure 4.6: Code name base3; $B=6.5\text{m}$; $B/D = 0.615$

4. Comparison with Centrifuge Experiment

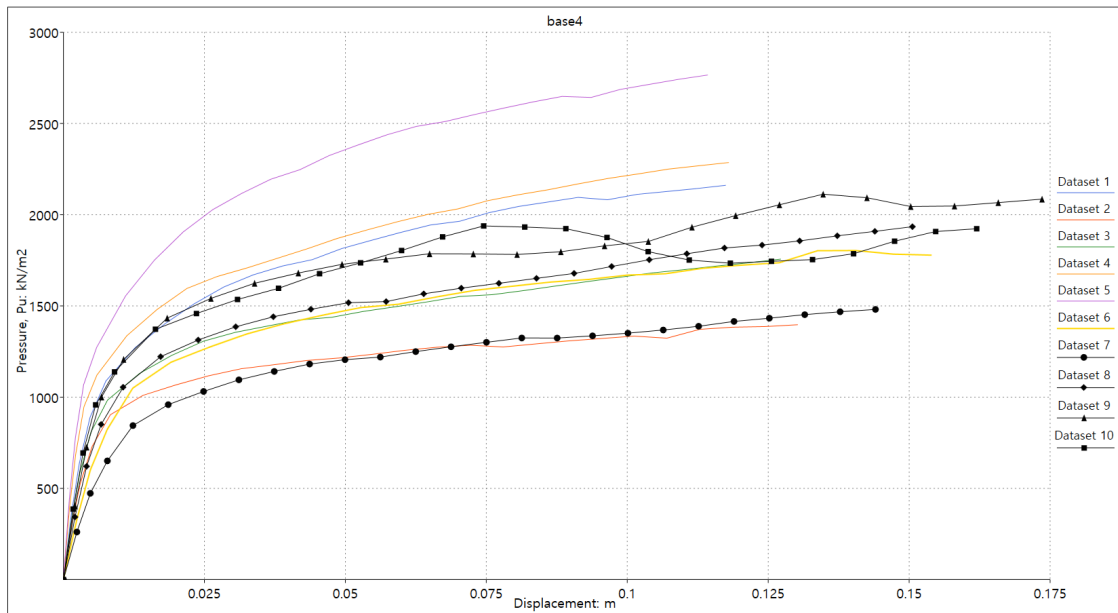


Figure 4.7: Code name base4; $B=4.5\text{m}$; $B/D = 1.044$

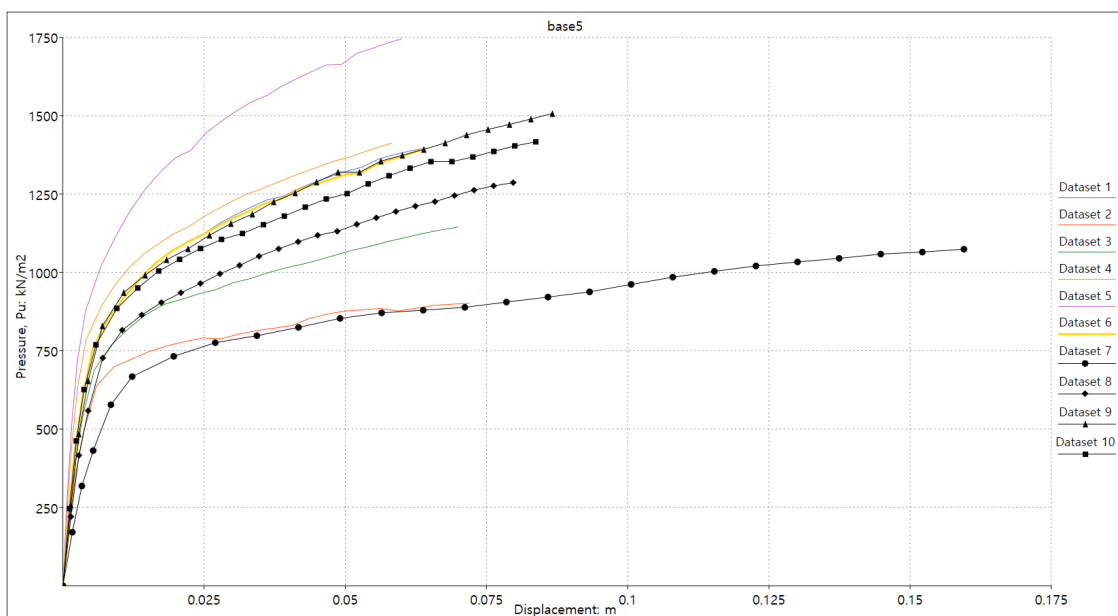


Figure 4.8: Code name base5; $B=4.5\text{m}$; $B/D = 0.744$

4. Comparison with Centrifuge Experiment

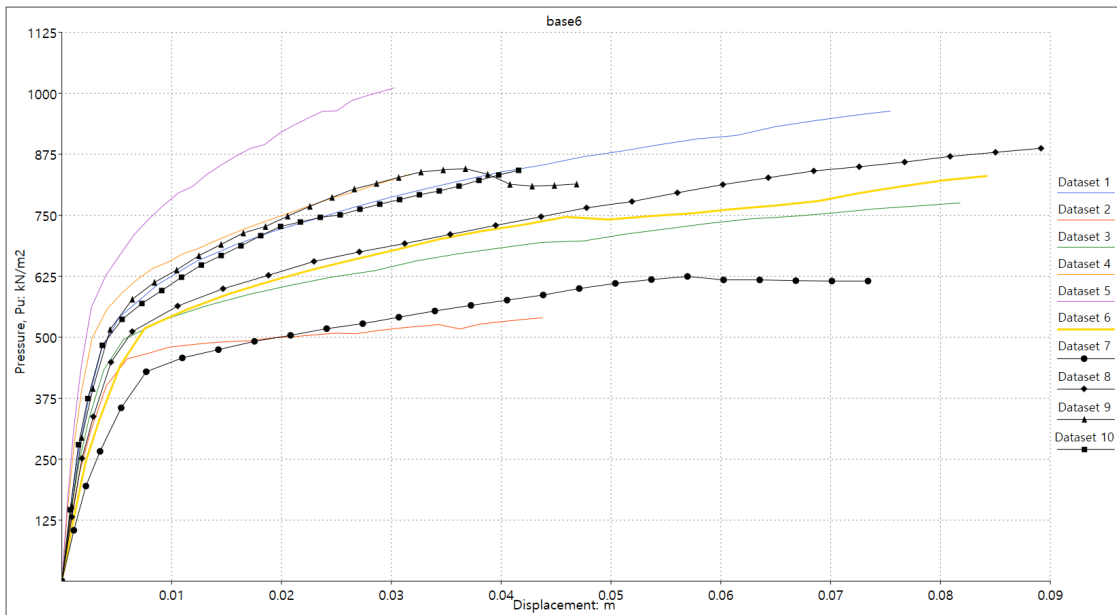


Figure 4.9: Code name base6; $B=4.5\text{m}$; $B/D = 0.444$

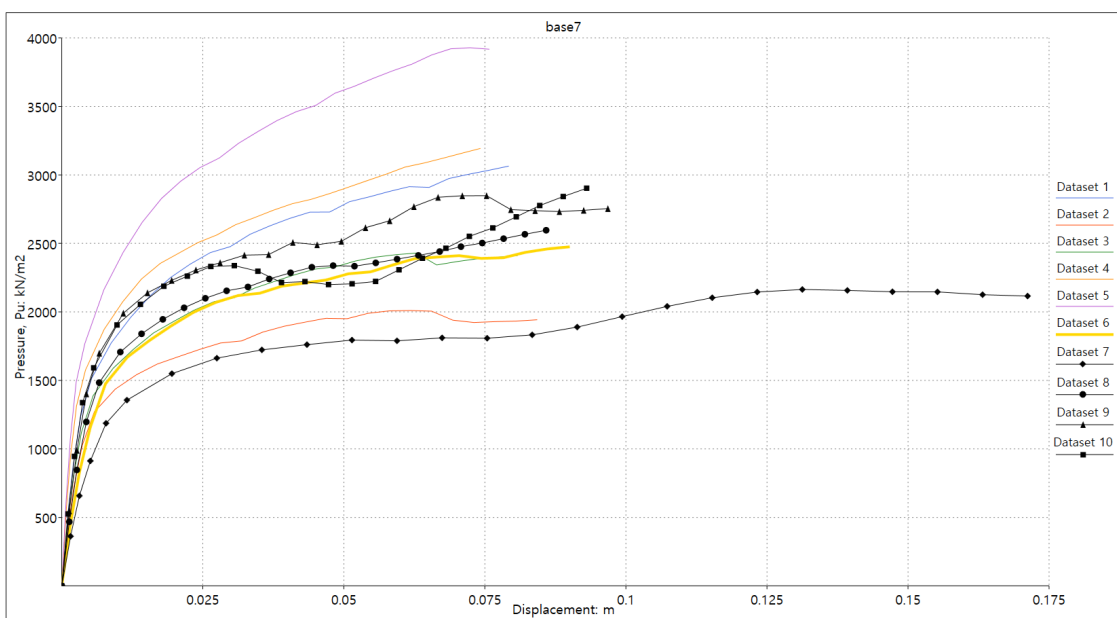


Figure 4.10: Code name base7; $B=3.5\text{m}$; $B/D = 1.314$

4. Comparison with Centrifuge Experiment

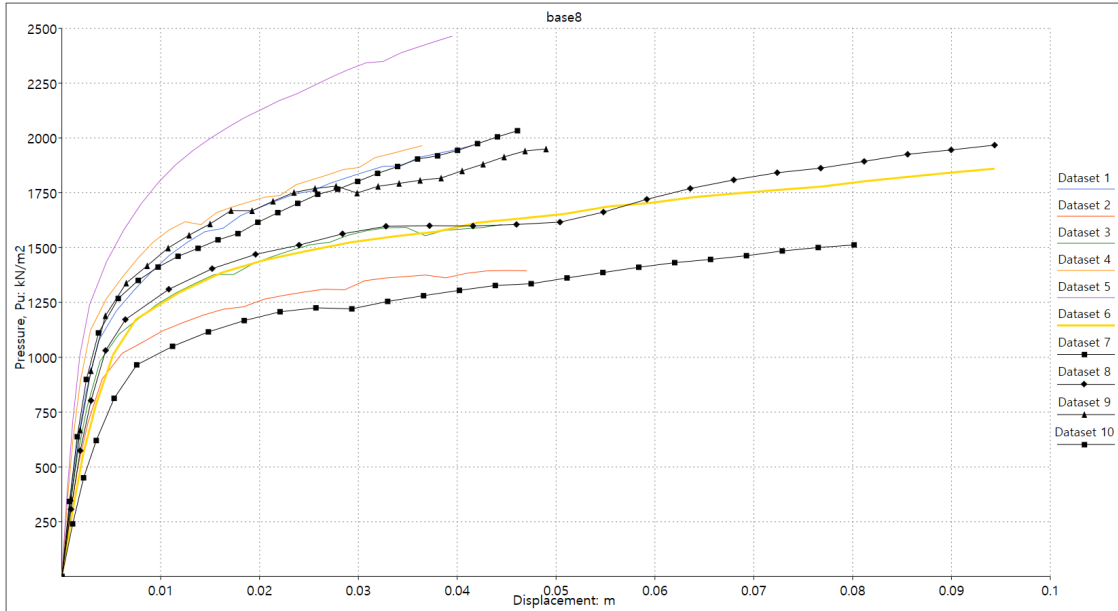


Figure 4.11: Code name base8; B=3.5m; B/D = 0.101

Determination of model parameters

To evaluate the difference between the centrifuge test result and the model prediction, residual error was used:

$$Error = \left| \frac{y_{actual} - y_{estimated}}{y_{actual}} \right| \times 100\%$$

The goal is to find the model which best fits (or has the least error) the measured data. For the dense sand cases, Model C and H, whereas for the loose sand cases, Model B and G were chosen for the further studies.

4. Comparison with Centrifuge Experiment

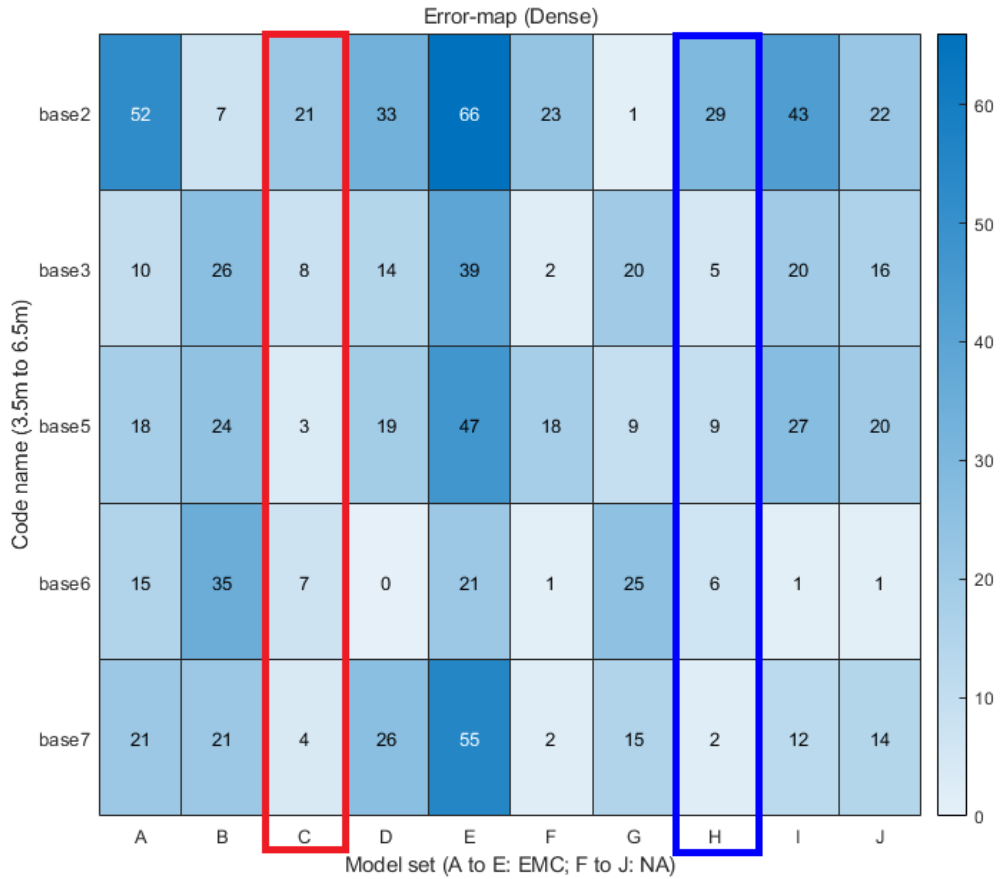


Figure 4.12: Heat-map of errors between centrifuge test and model (dense cases); model C and H were selected among available 10 models

4. Comparison with Centrifuge Experiment

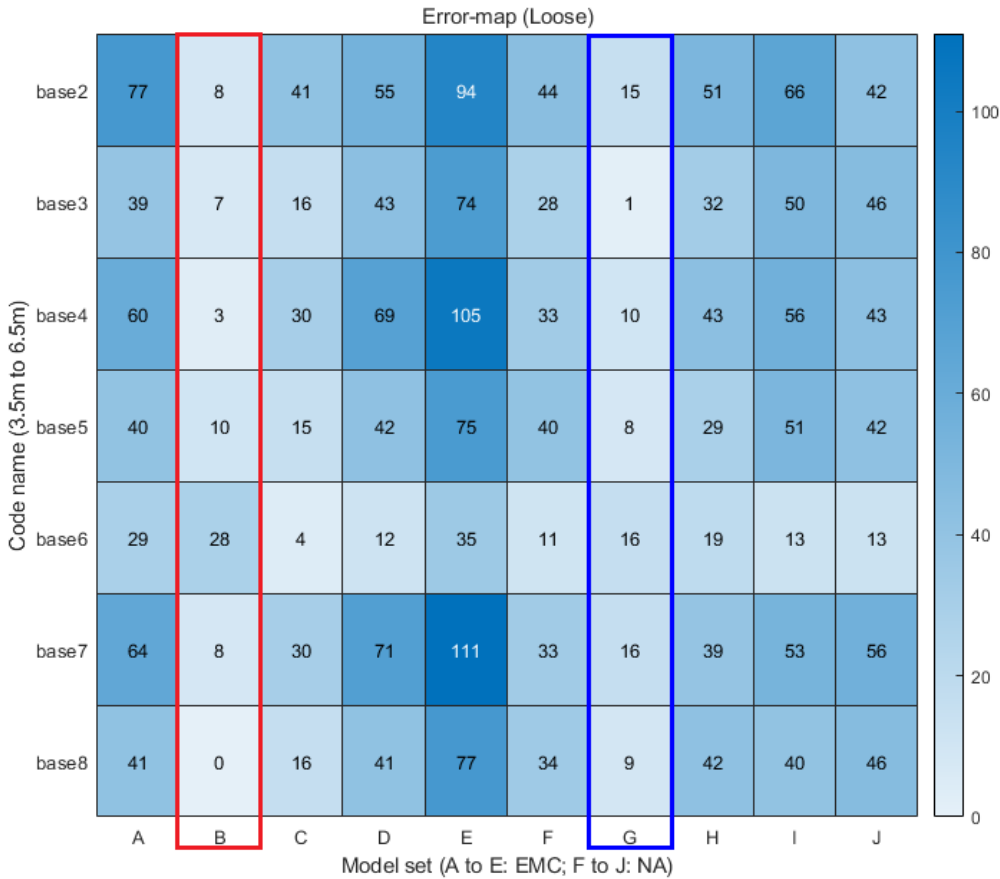


Figure 4.13: Heat-map of errors between centrifuge test and model (loose cases); model B and G were selected among 10 available models

4.1 Comparison of the centrifuge test results with the chosen model

The bar-chart was drawn to show the performance of the prediction of the EMC

and NA models with the centrifuge test results:

4. Comparison with Centrifuge Experiment

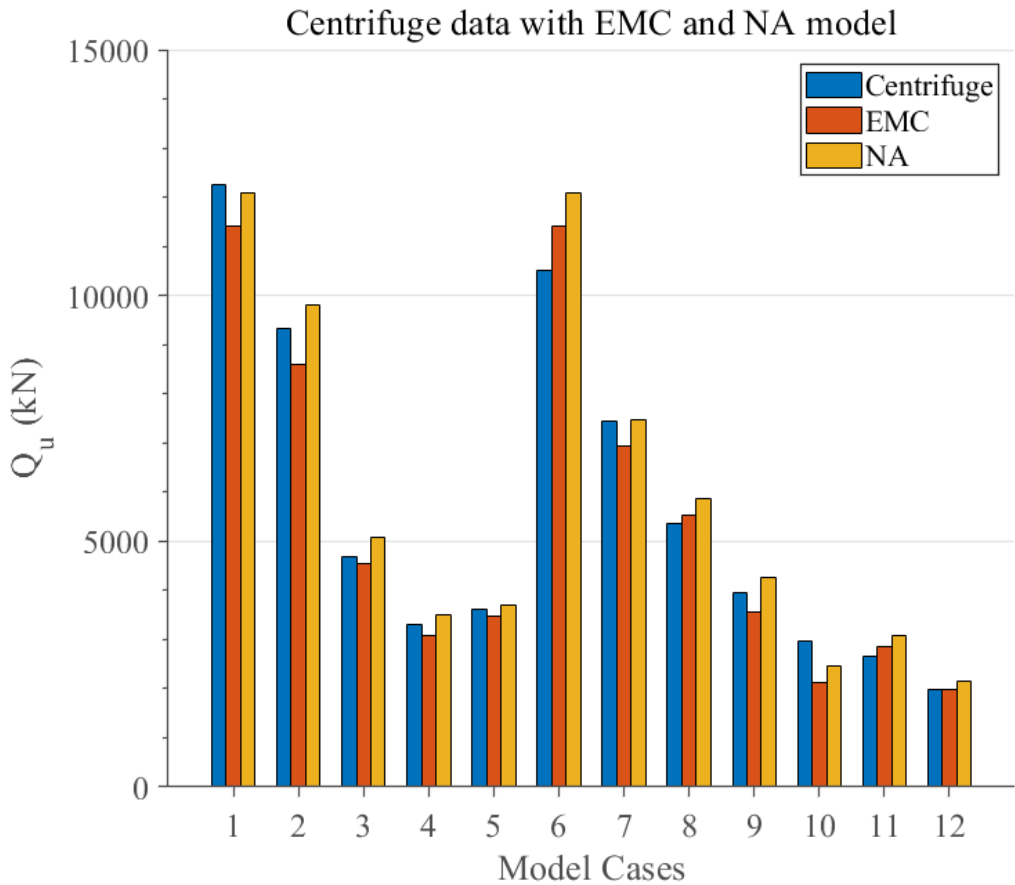


Figure 4.14: Bar-chart of centrifuge test and model (all cases); from left to right, 1: $B=6.5m, D/B=1.3$; 2: $B=6.5m, D/B=1$; 3: $B=4.5m, D/B=1.3$; 4: $B=4.5m, D/B=1$; 5: $B=3.5m, D/B=1.6$; 6: $B=6.5m, D/B=1.3$; 7: $B=6.5m, D/B=1$; 8: $B=4.5m, D/B=1.6$; 9: $B=4.5m, D/B=1.3$; 10: $B=4.5m, D/B=1$; 11: $B=3.5m, D/B=1.6$; 12: $B=3.5m, D/B=1.3$

Result of load—displacement curves of the centrifuge measurement with EMC and NA models

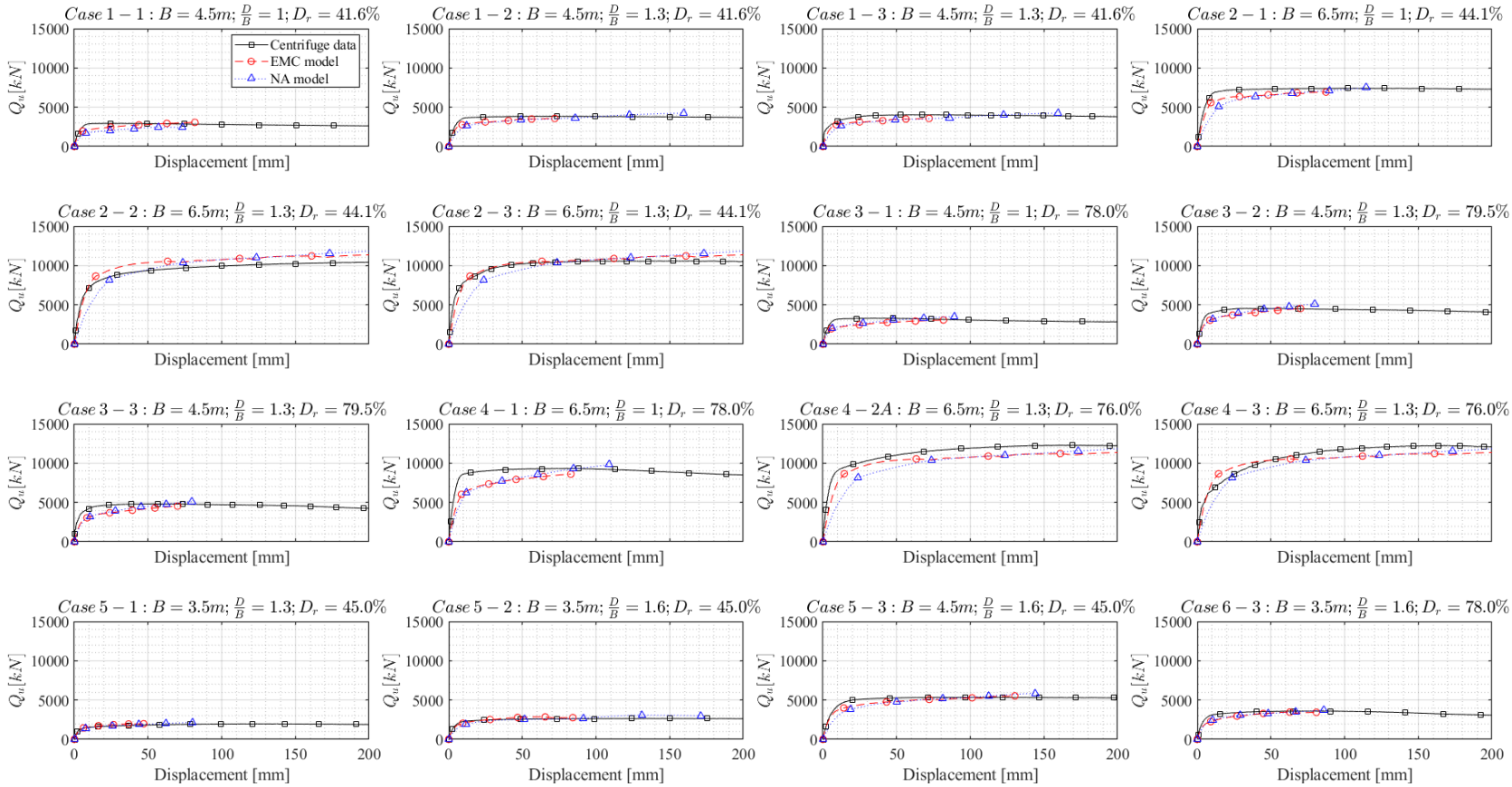


Figure 4.15: Comparison of centrifuge data with EMC and NA models

4. Comparison with Centrifuge Experiment

4.2 Difference with the anchor theory

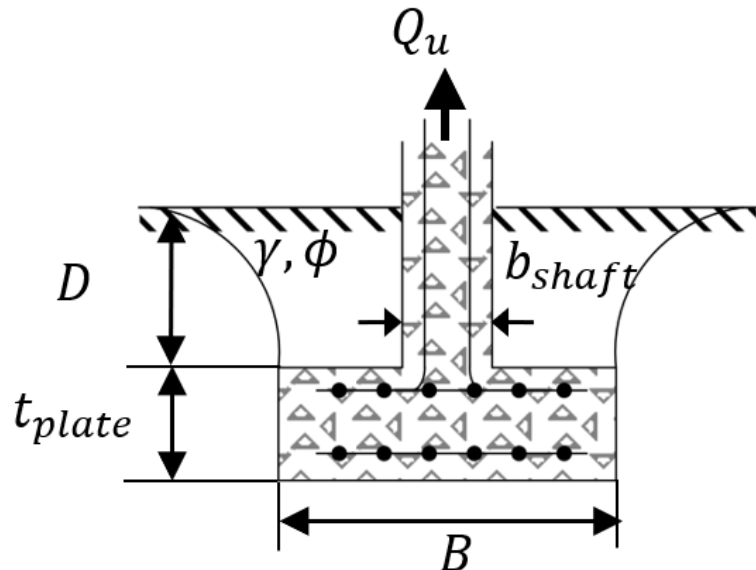


Figure 4.16: Schematic of typical shallow foundation

Dimensionless uplift capacity factor can be defined as the ratio of the ultimate uplift capacity to the soil encapsulated above the plate which lay inside the failure surface.

$$N_q = \frac{Q_u}{\gamma AD}$$

where A is area above the slab plate and can be calculated as $A = B^2 - \pi b_{shaft}^2$.

Effect of shaft diameter on dimensionless uplift capacity factor

For purpose of demonstrating difference between the anchor theory and that for the shallow foundations, dimensionless parameters were defined:

$$\lambda := \frac{b_{shaft}}{B}$$

4. Comparison with Centrifuge Experiment

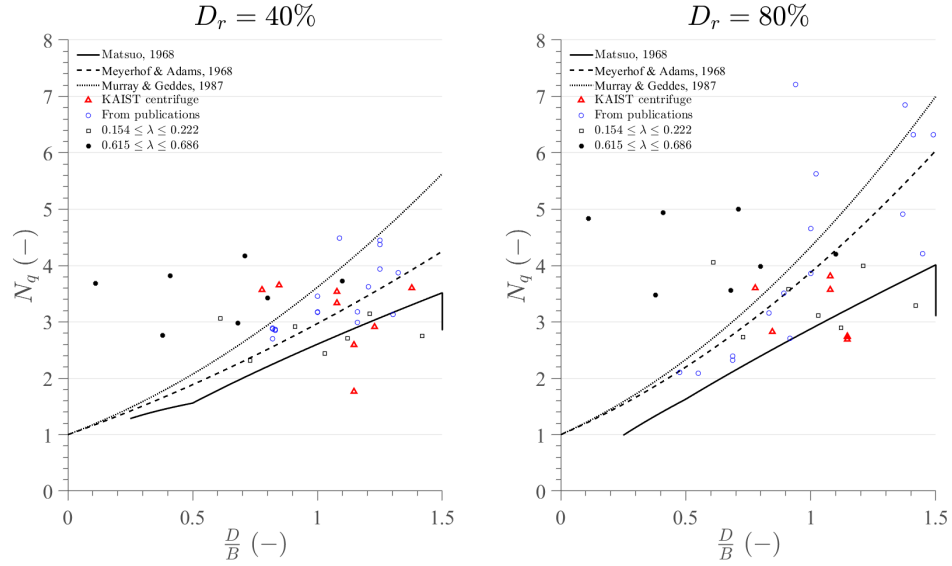


Figure 4.17: Comparison of theoretical and numerical models

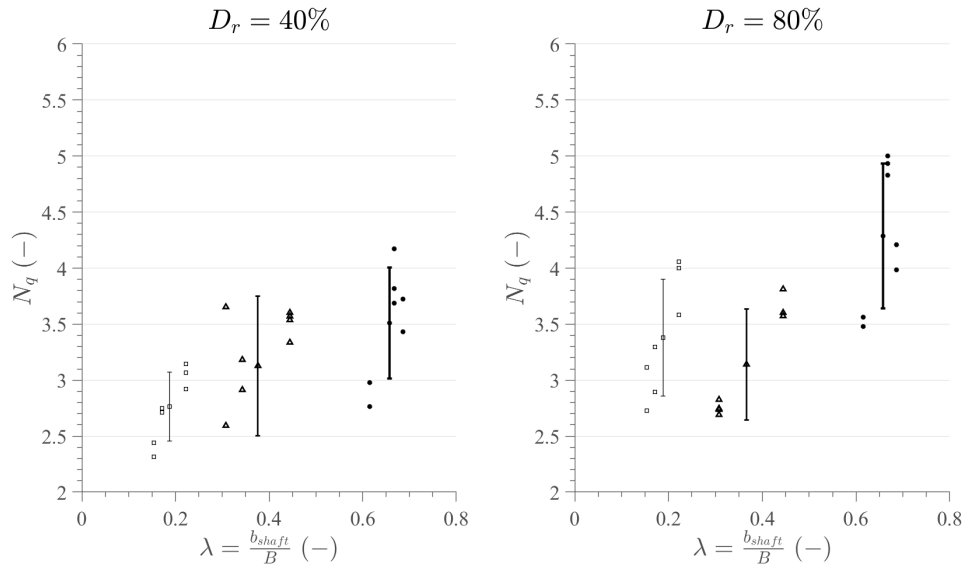


Figure 4.18: Comparison of theoretical and numerical models (variation on shaft diameter)

Effect of thickness on dimensionless uplift capacity factor

$$\mu := \frac{t_{plate}}{B}$$

4. Comparison with Centrifuge Experiment

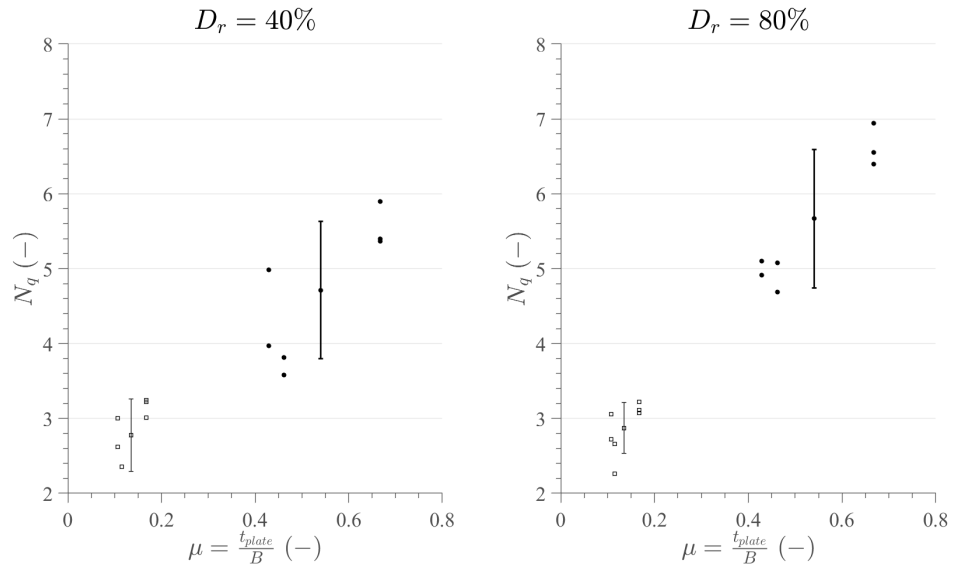


Figure 4.19: Comparison of theoretical and numerical models (variation on thickness)

Appendices

A

List of Load—Displacement Curves

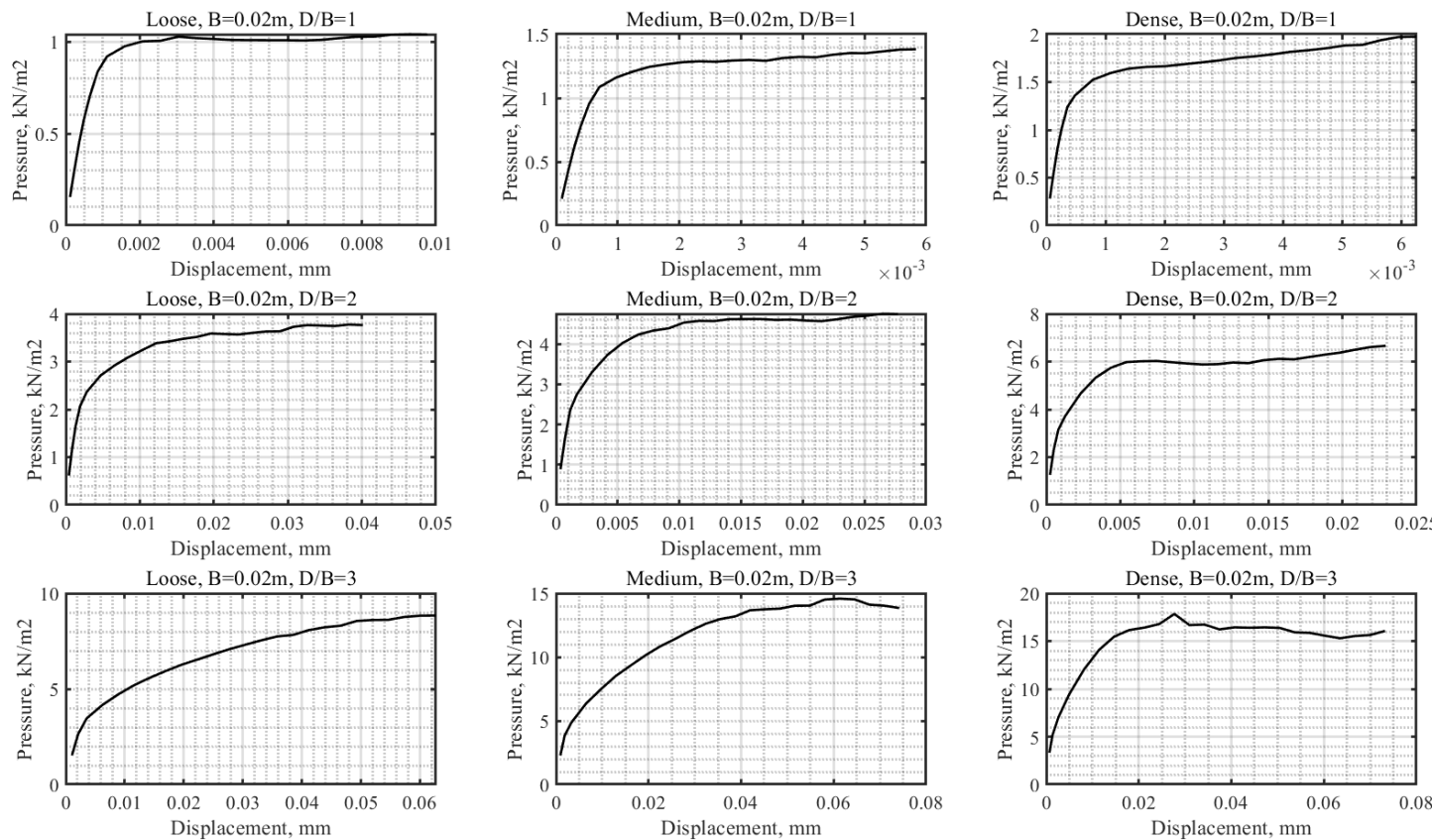


Figure A.1: Cumulative load-displacement curves of uplift of plate anchor in loose, medium, dense sands; D/B = 1,2,3; B=0.02m

A. List of Load—Displacement Curves

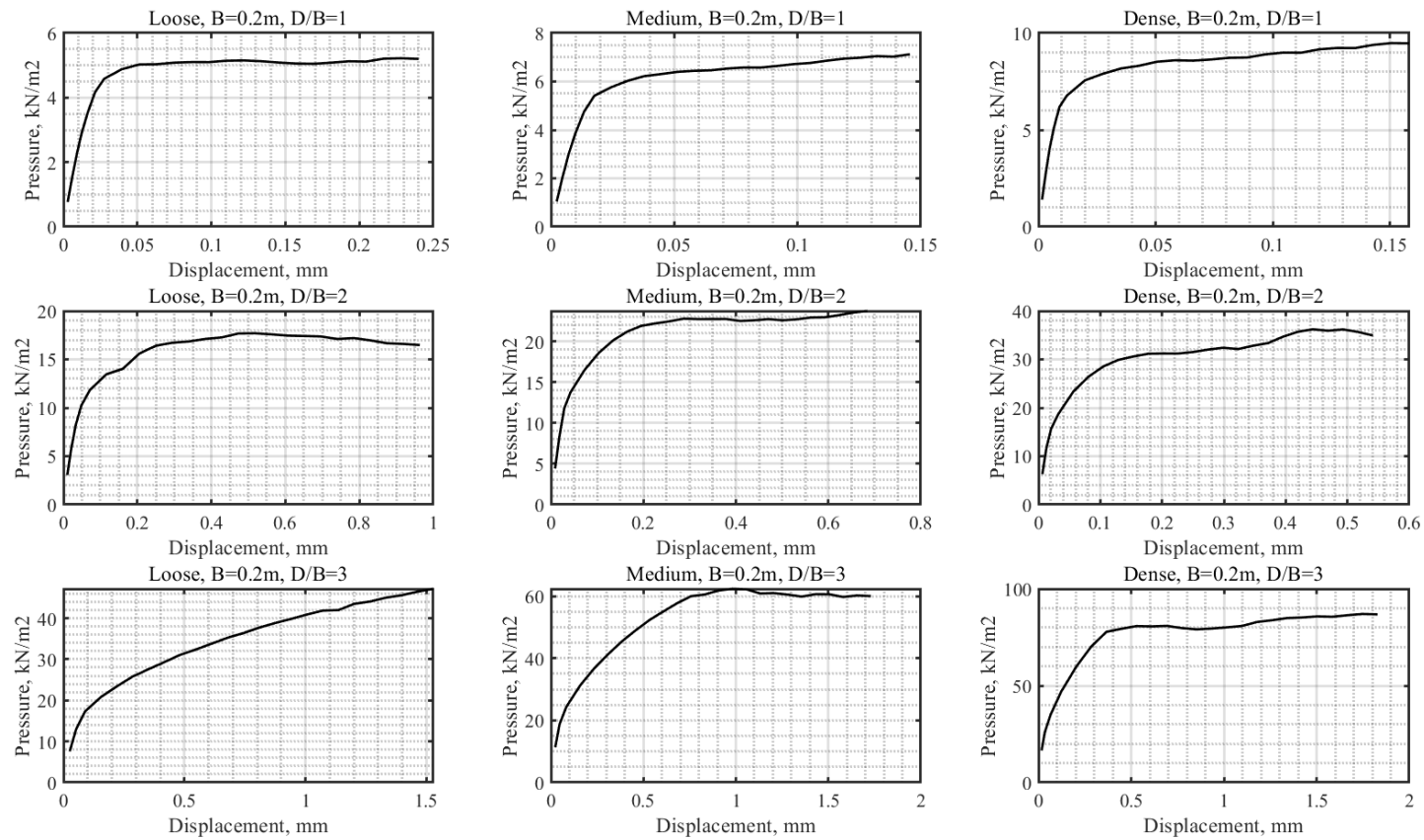


Figure A.2: Cumulative load-displacement curves of uplift of plate anchor in loose, medium, dense sands; D/B = 1,2,3; B=0.2m

A. List of Load—Displacement Curves

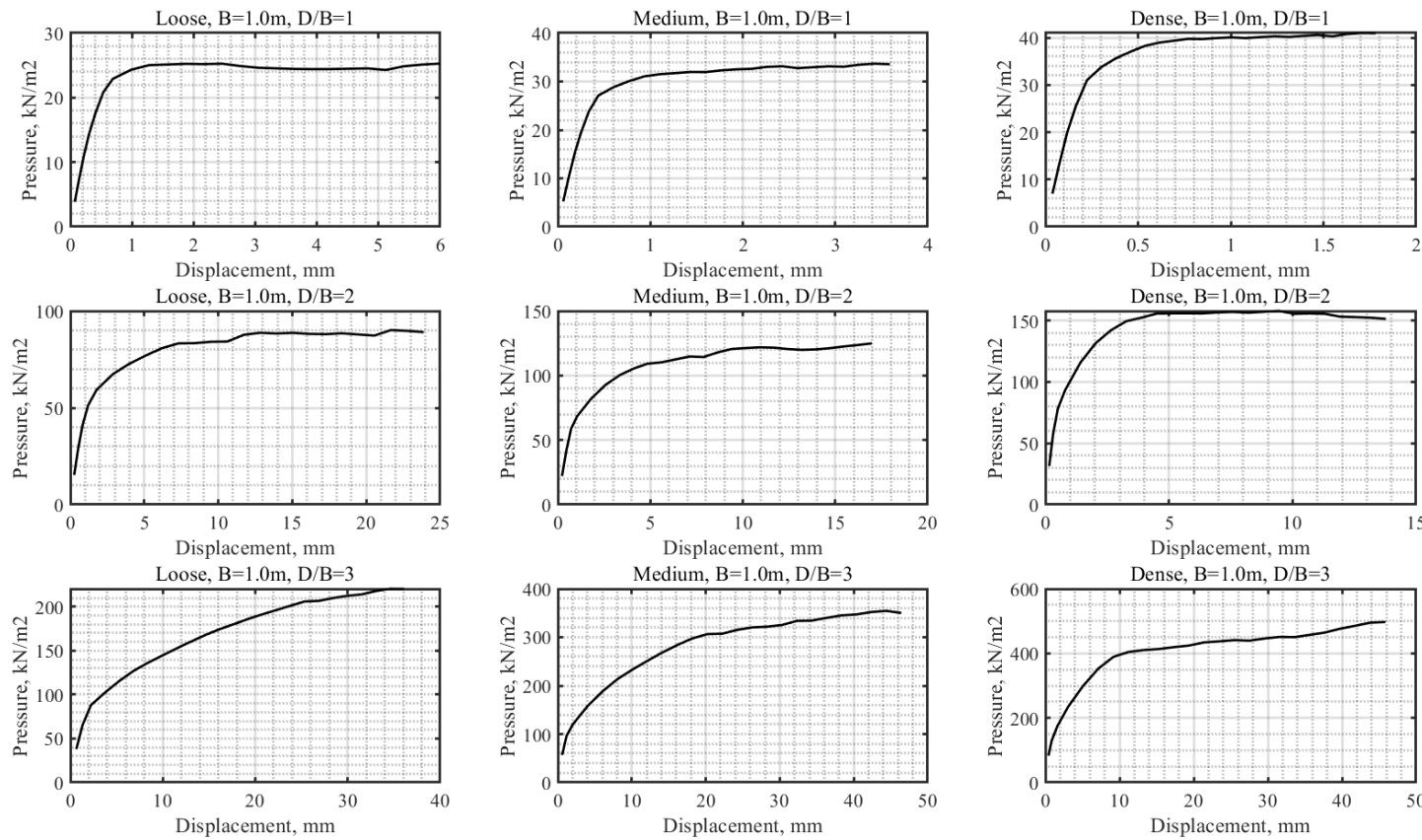


Figure A.3: Cumulative load-displacement curves of uplift of plate anchor in loose, medium, dense sands; $D/B = 1,2,3$; $B=1.0\text{m}$

A. List of Load—Displacement Curves

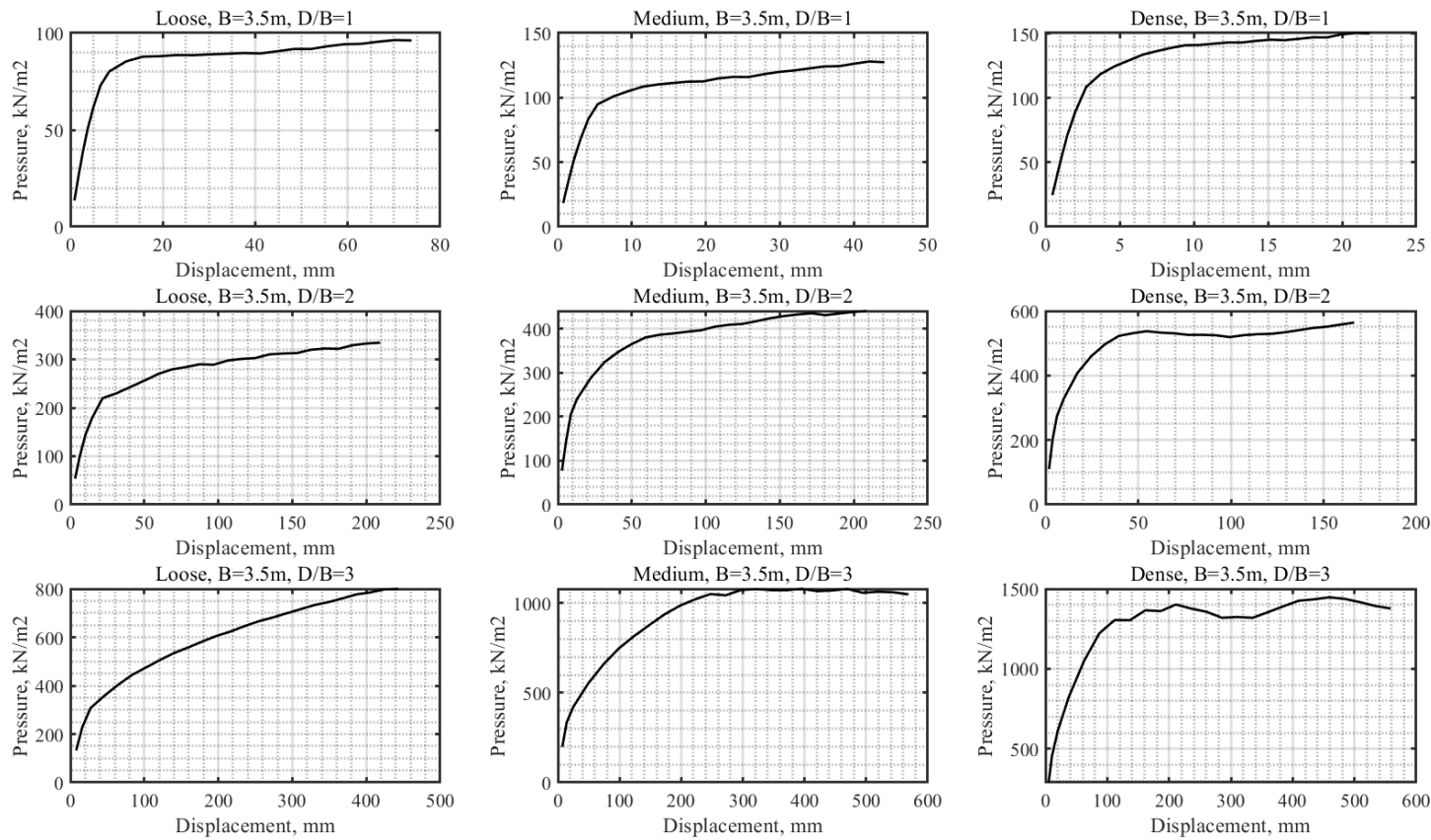


Figure A.4: Cumulative load-displacement curves of uplift of plate anchor in loose, medium, dense sands; $D/B = 1,2,3$; $B=3.5m$

A. List of Load—Displacement Curves

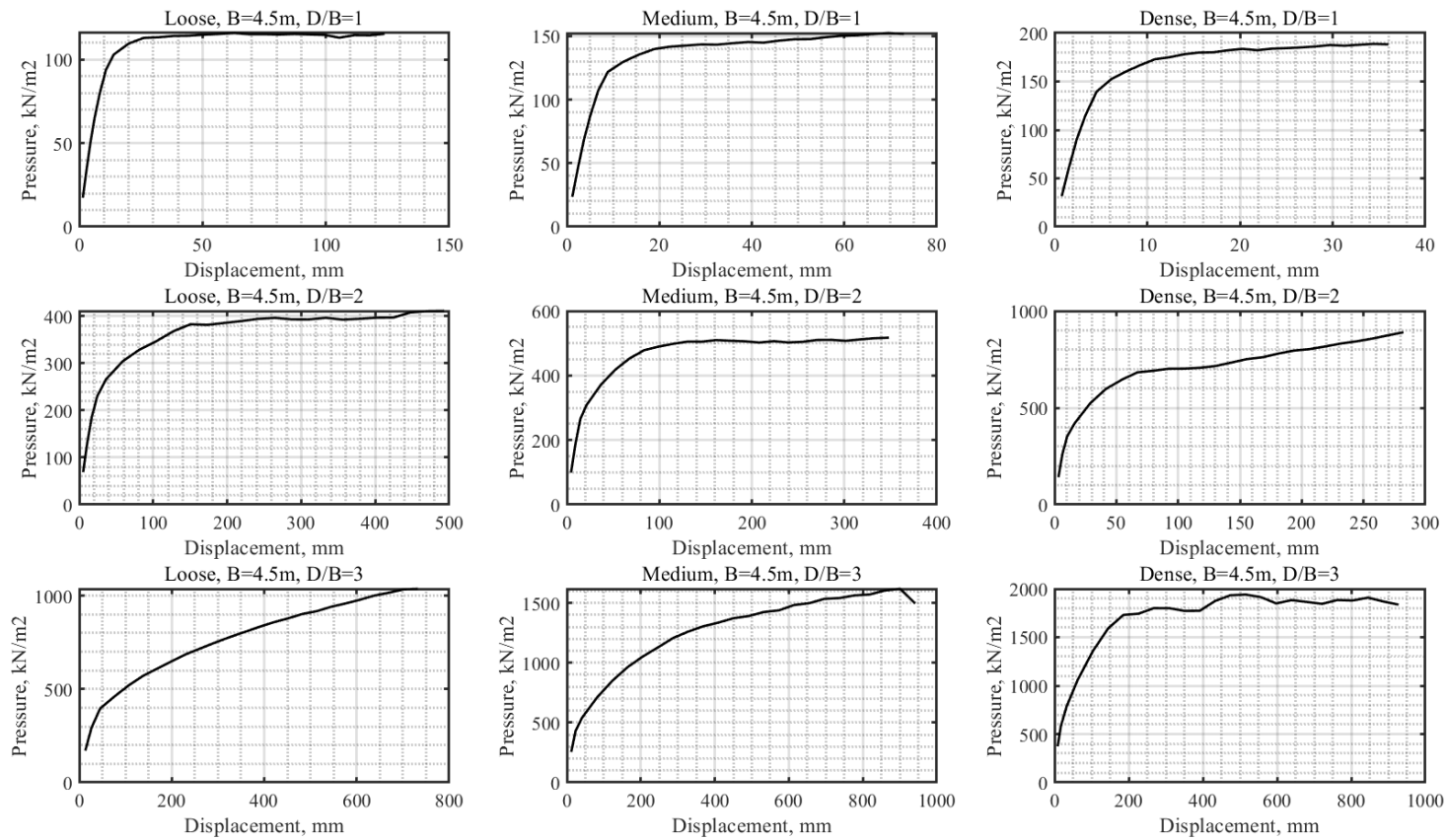


Figure A.5: Cumulative load-displacement curves of uplift of plate anchor in loose, medium, dense sands; D/B = 1,2,3; B=4.5m

A. List of Load—Displacement Curves

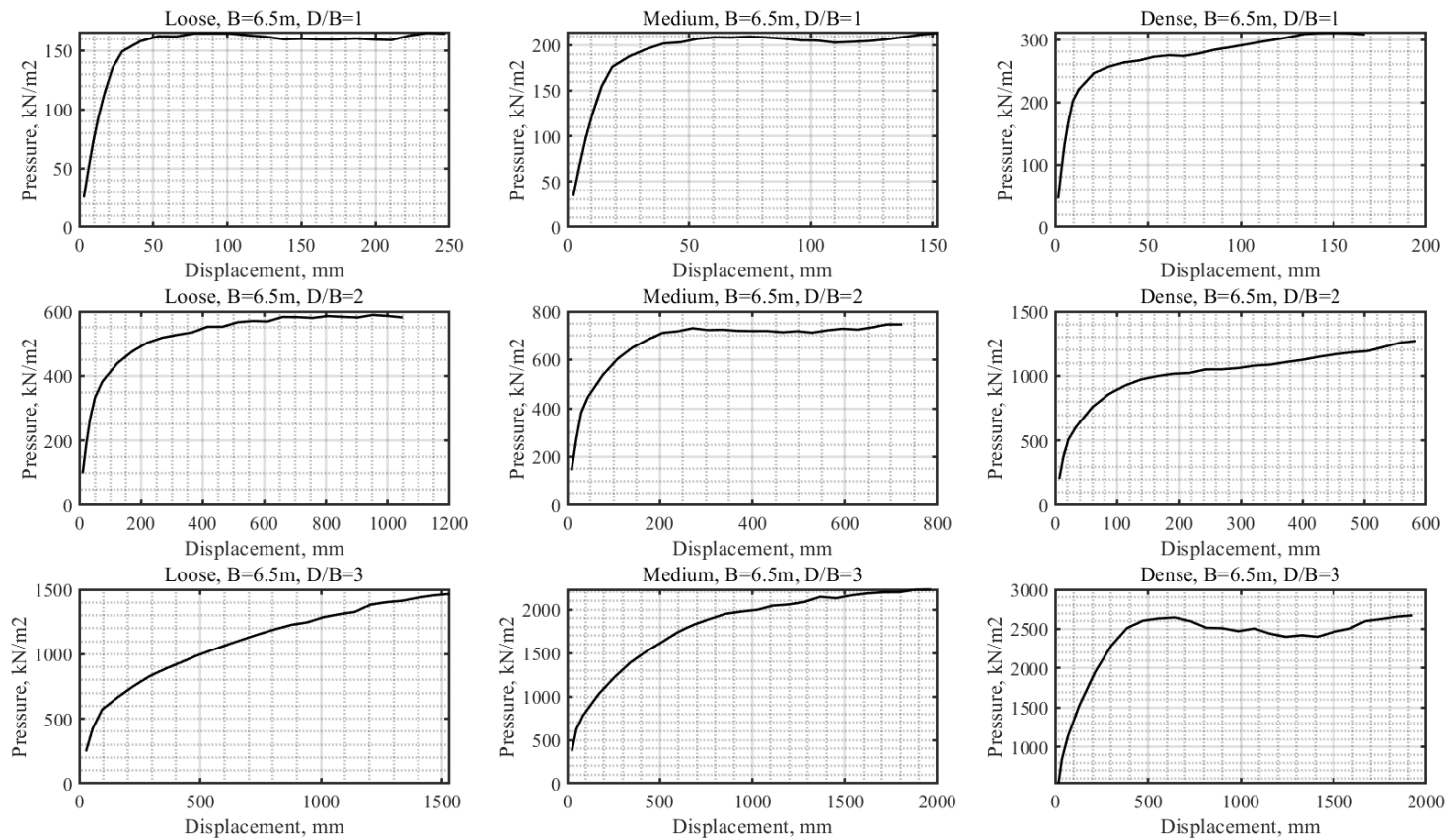


Figure A.6: Cumulative load-displacement curves of uplift of plate anchor in loose, medium, dense sands; D/B = 1,2,3; B=6.5m

B

REFERENCES

Wood, D. M. (2017). Geotechnical modelling. CRC press.

Doherty, J. P., & Muir Wood, D. (2013). An extended Mohr–Coulomb (EMC) model for predicting the settlement of shallow foundations on sand. *Géotechnique*, 63(8), 661-673.

Gajo, A., & Wood, M. (1999). Severn–Trent sand: a kinematic-hardening constitutive model: the q–p formulation. *Géotechnique*, 49(5), 595-614.

Krabbenhoft, S., Krabbenhoft, K., & Christensen, R. Limit analysis of the bearing capacity of strip-and circular footings on a layer of sand overlying clay.

Sakai, T., & Tanaka, T. (2007). Experimental and numerical study of uplift behavior of shallow circular anchor in two-layered sand. *Journal of geotechnical and geoenvironmental engineering*, 133(4), 469-477.

Tanaka, T., & Sakai, T. (1993). Progressive failure and scale effect of trap-door problems with granular materials. *Soils and Foundations*, 33(1), 11-22.

Sakai, T., & Tanaka, T. (1998). Scale effect of a shallow circular anchor in dense sand. *Soils and Foundations*, 38(2), 93-99.

B. REFERENCES

- Sakai, T., & Tanaka, T. (2007). Experimental and numerical study of uplift behavior of shallow circular anchor in two-layered sand. *Journal of geotechnical and geoenvironmental engineering*, 133(4), 469-477.
- Riyad, A. S. M., Rokonuzzaman, M., & Sakai, T. (2020). Progressive failure and scale effect of anchor foundations in sand. *Ocean Engineering*, 195, 106496.
- Kumar, J., & Kouzer, K. M. (2008). Vertical uplift capacity of horizontal anchors using upper bound limit analysis and finite elements. *Canadian Geotechnical Journal*, 45(5), 698-704.
- Riyad, A. S. M., Rokonuzzaman, M., & Sakai, T. (2020). Effect of using different approximation models to the exact Mohr–Coulomb material model in the FE simulation of Anchor Foundations in sand. *International Journal of Geo-Engineering*, 11(1), 1-21.
- Riyad, A. S. M., Rokonuzzaman, M., & Sakai, T. (2020). Progressive failure and scale effect of anchor foundations in sand. *Ocean Engineering*, 195, 106496.
- Roy, A., Chow, S. H., O'Loughlin, C. D., & Randolph, M. F. (2021). Towards a simple and reliable method for calculating uplift capacity of plate anchors in sand. *Canadian Geotechnical Journal*, 58(9), 1314-1333.